HHS Public Access

Author manuscript

Nature. Author manuscript; available in PMC 2019 June 07.

Published in final edited form as:

Nature. 2018 September ; 561(7721): 70–75. doi:10.1038/s41586-018-0469-4.

Malaria Parasite Translocon Structure and Mechanism of Effector Export

Chi-Min Ho[1,2,3], **Josh R. Beck**[4,5], **Mason Lai**[2], **Yanxiang Cui**[6], **Daniel E. Goldberg**[4], **Pascal F. Egea**[1,3,*], and **Z. Hong Zhou**[1,2,6,*]

[1]The Molecular Biology Institute, University of California, Los Angeles, CA 90095, USA

[2]Department of Microbiology, Immunology, & Molecular Genetics, University of California, Los Angeles, CA 90095, USA

[3]Department of Biological Chemistry, David Geffen School of Medicine, University of California, Los Angeles, CA 90095, USA

[4]Departments of Medicine and Molecular Microbiology, Washington University School of Medicine, St. Louis, MO 63110, USA

[5]Department of Biomedical Sciences, Iowa State University, Ames, IA 50011, USA

[6]California NanoSystems Institute, University of California, Los Angeles, CA 90095, USA

Summary

The putative *Plasmodium* Translocon of Exported Proteins (PTEX) is essential for transport of malarial effector proteins across a parasite-encasing vacuolar membrane into host erythrocytes, but the mechanism of this process remains unknown. Here we show PTEX is a *bona fide* translocon by determining near-atomic resolution cryoEM structures of the endogenous PTEX core complex of EXP2, PTEX150 and HSP101, isolated from *Plasmodium falciparum* in the *engaged* and *resetting* states of endogenous cargo translocation with CRISPR/Cas9-engineered epitope tags. EXP2 and PTEX150 interdigitate to form a static, funnel-shaped pseudo-sevenfold symmetric protein-conducting channel spanning the vacuolar membrane. Tethered above this funnel, the spiral-shaped AAA+ HSP101 hexamer undergoes a dramatic compaction that allows three of six tyrosine-bearing pore loops lining the HSP101 channel to dissociate from the cargo, resetting the

*Correspondence and request for materials should be addressed to Z.H.Z. (Hong.Zhou@UCLA.edu, for cryoEM and atomic modeling) and P.F.E. (PEgea@mednet.ucla.edu, for biochemistry).

Contributions

CMH, PFE and ZHZ initiated the project; JRB generated parasite lines, harvested parasites, performed complementation experiments and helped write the paper; CMH purified the sample, screened purified samples by negative stain, prepared cryoEM grids, acquired and processed the cryoEM data, interpreted the structures and wrote the paper; ML built and refined the atomic models and helped interpret the structures; YC helped with sample freezing; ZHZ supervised the cryoEM aspects of the project, interpreted the structures and wrote the paper; PFE supervised biochemical aspects of the project and helped interpret the structures; DEG supervised parasitology aspects of the project. DEG, ML, and PFE helped edit the paper.

Data availability

The atomic models and the cryoEM density maps are deposited to the Protein Data Bank and the Electron Microscopy Data Bank, under the accession numbers 6E10, 6E11, EMD-8951 and EMD-8952.

Competing interests

The authors declare no competing interests.

translocon for the next threading cycle. Our work reveals the mechanism of *P. falciparum* effector export, enabling structure-based design of drugs targeting this unique translocon.

Malaria has devastated major civilizations since the dawn of humanity and remains a significant burden to our society, responsible for nearly half a million deaths annually[1]. This infectious disease is caused by *Plasmodium* parasites, which invade and reproduce within human erythrocytes, inducing the clinical symptoms of malaria[2,3]. These parasites export hundreds of effector proteins to extensively remodel host erythrocytes, which have limited capacity for biosynthesis[4–6]. Collectively known as the exportome, these proteins create the infrastructure necessary to import nutrients, export waste, and evade splenic clearance of infected erythrocytes[7]. Most of these proteins bear a 5-residue motif, the *Plasmodium* Export Element (PEXEL)[8–10]. The malaria parasite conceals itself inside a parasitophorous vacuole (PV) derived from invagination of the host cell plasma membrane during invasion[11] (Fig. 1a). Following secretion into the PV, proteins destined for export are unfolded and transported across the PV membrane (PVM) into the host cell in an ATP-dependent process[12,13]. To accomplish this, it was proposed that the parasite has evolved a unique membrane protein complex, the *Plasmodium* Translocon of Exported Proteins (PTEX)[14]. PTEX is the only known point of entry to the host cell for exported proteins and an attractive drug target, as disrupting PTEX blocks delivery of key virulence determinants, inducing parasite death[15,16].

PTEX was suggested to be a >1.2MDa membrane protein complex with a core composed of the HSP101 ATPase and two novel proteins, PTEX150 and EXP2 (Fig. 1a)[14,17]. HSP101 belongs to the Class 1 Clp/HSP100 family of AAA+ ATPases, PTEX150 has no known homologs beyond the *Plasmodium* genus, and EXP2 is a PVM protein[14,18] conserved among vacuole-dwelling apicomplexans[19]. All three core components are essential for protein export and parasite survival[15,16,20]. A model of PTEX-mediated translocation was proposed in which HSP101 unfolds and threads proteins through an oligomeric EXP2 transmembrane channel spanning the PVM, with PTEX150 playing a structural role between EXP2 and HSP101[14–17]. However, without structural information, the global architecture of PTEX, the stoichiometry of its components, and direct evidence for the proposed molecular mechanism have proven elusive.

In this study, we purify PTEX directly from the human malaria parasite *P. falciparum* and determine near-atomic resolution cryoEM structures of the complex in multiple functional states. Our atomic models reveal the architecture and mechanism of this unique translocon and pave the way for development of novel therapeutics against this promising new malarial drug target.

Architecture of the PTEX core complex

To purify PTEX from *P. falciparum*, we used CRISPR/Cas9 editing to introduce a 3xFLAG epitope tag on the endogenous HSP101 C-terminus (Extended Data Fig. 1a–c) and purified the endogenously assembled PTEX core complex directly from parasites cultured in human erythrocytes (Extended Data Fig. 1d–f). CryoEM analysis yielded two distinct conformations of PTEX particles, one extended (195Å) and the other compact (175Å) (Fig.

1b-c). Endogenous cargo polypeptide densities are visible in the central pore of HSP101 in both structures (Fig. 1b-c, Extended Data Fig. 2–3). Based on differences in the arrangement of HSP101 subunits relative to the cargo between the two conformations, we designated them as the *engaged* and *resetting* states, respectively. Both maps are at near-atomic resolution, varying from 3–3.6Å in the transmembrane (TM) and core regions to 5–8Å in the periphery (Fig. 1b-c, Extended Data Fig. 4). Clear sidechain densities throughout most regions of both maps (Fig. 1b-c, Extended Data Fig. 5, Supplementary Videos 1–2) enabled us to build *de novo* atomic models of the three constituent proteins for both conformational states (Fig. 1d-e), each containing 20 subunits with 6,898 amino acid residues modeled. All subunits were built independently, as conformations varied between subunits.

Both structures reveal PTEX to be a tripartite membrane protein complex with a 6:7:7 stoichiometry and a calculated mass of 1.6MDa, composed of a hexameric HSP101 protein-unfolding motor tethered to a PVM-spanning, pseudosymmetric funnel formed by seven protomers of EXP2 interdigitating with seven protomers of PTEX150 (Fig. 1d–k, Supplementary Video 3). Two transiently associated[21] accessory proteins, PTEX88 and TRX2[14], are not observed in our structures. At the PVM, each EXP2 monomer contributes a single TM helix to form a sevenfold (C7)-symmetric protein-conducting channel spanning the membrane (Fig. 1j-k). Six HSP101 protomers are tethered atop the PTEX150/EXP2 funnel in a hexameric right-handed spiral, with a gap between the bottom-most and top-most protomers (Fig. 1f-g, Supplementary Video 4). The HSP101 hexamer is oriented such that a single unbroken channel extends from the top of the HSP101 hexamer to the bottom of the heptameric EXP2 transmembrane pore (Fig. 1l–n, Extended Data Fig. 2d). The most constricted point along the channel occurs in HSP101, measuring 4Å and 10Å in diameter, in the *engaged* and *resetting* states, respectively (Fig. 1l). The seventh EXP2 and PTEX150 protomers are situated beneath the gap between HSP101 protomers 1 and 6, accommodating the remarkable symmetry mismatch between the asymmetric HSP101 hexamer and the pseudo-sevenfold-symmetric PTEX150/EXP2 tetradecamer (Fig. 1f-k, Extended Data Fig. 2e–j). Analyses of our PTEX150 and EXP2 structures with four commonly used structural similarity search programs[22–25] revealed no consistent structural similarities to any known proteins, including the pore-forming toxin Hemolysin E (HlyE), with which EXP2 was previously speculated to share structural homology[14]. Below, we describe the structural details of the individual proteins in the *engaged* state, followed by a comparison of the two states that suggests a mechanism of translocation.

EXP2 forms a heptameric protein-conducting channel across the PVM

Residues G27-S234 of EXP2 are well resolved in our structure, accounting for 80% of the mature protein (Extended Data Fig. 6a). EXP2 is a single-pass transmembrane protein consisting of a kinked 60Å-long N-terminal TM helix followed by a globular body domain and ending in an assembly domain composed of a linker helix followed by the assembly strand (Fig. 2a-b). The body domain contains five helices (B1–5), stabilized by an intraprotomer C113-C140 disulfide bond (Fig. 2c).

Seven EXP2 protomers (labeled A-G) oligomerize to form a funnel-shaped C7-pseudosymmetric 216kDa heptamer spanning the PVM (Fig. 2d–e). The TMD and body

helices B1–3 are symmetric throughout all seven protomers (Extended Data Fig. 3a-b). This symmetry is broken by inter-protomer conformational variations in body helices B4–5 and the assembly domain, which stretch upwards in some protomers to maintain contacts with the asymmetric HSP101 hexamer situated above the EXP2 funnel. This variation is most pronounced in EXP2 protomers F and G (Extended Data Fig. 3a-b).

In the EXP2 heptamer, the amphipathic TM helices twist slightly around each other, creating a 37Å-long C7-symmetric protein-conducting channel that spans the PVM and forms the stem of the funnel (Fig. 2d-e). The membrane-facing surface of the EXP2 channel is coated with hydrophobic residues, while the inner surface is lined with charged and polar residues, creating an aqueous pore (Fig. 2e). The body domains, positioned in a wider ring atop the transmembrane channel on the vacuolar face of the PVM, form the mouth of the funnel. This orientation is consistent with previous analyses of EXP2 topology[14,20]. Furthermore, a detergent belt is clearly visible in 2D class averages and density maps (Extended Data Fig. 7–8), defining the residues in the TMD that would be buried in the PVM. A ring of positively charged residues where the stem meets the mouth of the funnel is positioned to interact with the negatively charged phosphates of the membrane surface (Extended Data Fig. 8a).

The PTEX150(S668-D823) heptamer acts as an adaptor between HSP101 and EXP2

Of the 993 residues in PTEX150, S668-D823 are well resolved in our structure and form a hook with a shaft (Fig. 3a-b). The hook domain consists of three short helices (H1–3) joined by several long loops. Directly N-terminal and C-terminal to the hook domain, the shaft is composed of proximal and distal shaft domains (Fig. 3a-b). The remaining 80% of PTEX150, not visible in our structures, is predicted to be intrinsically disordered (average disorder tendency of 0.83 in IUPred[26,27], with scores above 0.5 indicating disorder), unlike the rigid structured core of PTEX150 (S668-D823) (average disorder tendency score of 0.42, indicating ordered structure), suggesting that this 80% of the protein is too mobile to be observed and may be flexibly arranged outside the stable PTEX core.

Seven PTEX150(S668-D823) hooks (labeled a-g) oligomerize, forming a flange-shaped C7-pseudosymmetric heptamer (Fig. 3c) that fits into the mouth of the EXP2 channel. Each hook lies in the groove between adjacent EXP2 body domains, and the tip of the hook curls down into the mouth of the EXP2 pore (Fig. 3d). A vertical, heptameric ring of H2 helices sits in the mouth of the EXP2 funnel, forming a conduit between the hexameric HSP101 and heptameric EXP2 central pores (Extended Data Fig. 2g–j). In this way, PTEX150(S668-D823) serves as an adaptor between HSP101 and EXP2, providing a continuous protected path for unfolded cargo.

Endogenous cargo is observed bound in the channel of the HSP101 protein unfoldase

Class 1 Clp/HSP100 AAA+ ATPases are highly conserved hexameric protein unfoldases associated with diverse functions, which are known to thread polymeric substrates through a central pore[28,29]. HSP101 is a 598kDa hexamer exemplifying the canonical Class 1 Clp/HSP100 domain architecture[30,31], with a substrate-binding N-terminal domain (NTD)[32] followed by two AAA+ nucleotide-binding domains (NBD1 and NBD2), each containing a cargo-binding pore loop (L1 and L2, respectively) that extends into the central pore (Fig. 4a-b). Additionally, HSP101 contains a C-terminal domain (CTD), and a coiled-coil middle domain (MD) insertion in the C-terminal end of NBD1 (Fig. 4a-b).

Unlike Class 2 HSP100s [Ref 33], Class 1 HSP100s form three-tiered hexamers, where the NTDs, NBD1s and NBD2s form the top, middle, and bottom tiers, respectively[30,31]. In our *engaged* state structure, the NBD1 and NBD2 tiers are arranged in a right-handed ascending spiral[30,31,34] (Fig. 4c). A layer of weaker density above the NBD1 tier may correspond to the NTDs, which are likely dynamic (Extended Data Fig. 8b). The MDs encircle the upper NBD1 tier. The central pore of the spiral is lined with pore loops bearing tyrosines in a spiral staircase pattern. The tyrosine sidechain densities intercalate with a 45Å-long density clearly visible in the middle of the chaperone pore (Fig. 4c-d, Supplementary Video 5), which closely resembles unfolded cargo polypeptide densities reported in recently published cryoEM structures of homologous HSP100s bound to cargo[31,33] (Extended Data Fig. 2a–d). The unfolded PTEX cargo polypeptide chain modeled into this 45Å-long density matches very closely (RMSD of 1.09–1.25Å) with the unfolded cargo polypeptides in these cargo-bound homolog structures (Extended Data Fig. 2a–c).

Key interactions for PTEX assembly and a potential mechanism for regulation

While the three PTEX components share extensive binding interfaces, we describe only the two most intriguing interactions here. In EXP2 protomers A-F, the assembly strand augments the CTD β-sheet in the HSP101 protomer situated directly above (Fig. 5a-b). Protomer G occupies the space beneath the gap between HSP101 protomers 1 and 6 (Fig. 1f–k). This hydrogen bond-mediated interaction tethers the HSP101 hexamer to the transmembrane funnel, positioning the central pore exit directly above the entrance to the PTEX150/EXP2 pore. We hypothesized that this interaction is essential for assembly of the PTEX core complex, and that the complex must be stably assembled to be active. We tested this using genetic functional complementation in live parasites.

Knockdown of EXP2 produces a lethal defect in parasite growth and export that can be rescued by a mutant version of EXP2 lacking the last 54 residues[20]. Thus, the amino acids immediately following the assembly strand are not essential for PTEX function. However, complementation with a version of EXP2 lacking an additional 12 residues, removing the assembly strand, failed to rescue these phenotypes (Fig. 5c–f). These results demonstrate

that the EXP2 assembly strand is critical to PTEX function, consistent with an essential role in docking the HSP101 unfoldase to the EXP2 membrane channel to facilitate translocation.

A strong, albeit lower resolution claw-shaped density extends from the end of each modeled PTEX150(S668-D832) shaft to the HSP101 MD above, terminating in a three-turn helix resting atop the midpoint of the MD. This helix forms a strong interaction with HSP101 Y488 and Y491 in claws a-e (Extended Data Fig. 8d-e) but is not visible in claw f in the *engaged* state. Claw g appears to form an additional interaction with the N-terminal end of the HSP101 protomer 1 MD (Extended Data Fig. 8d). The MD is known to play a critical role in regulating ATPase and unfoldase activities in related HSP100s [Ref 35,36], suggesting the importance of this interaction.

Atomic details of the two observed states suggest a mechanism for translocation

In addition to the above-described *engaged* (195Å) state, a more compact (175Å) *resetting* state of PTEX was also observed. Much of PTEX150(S668-D823) and EXP2 remain unchanged between the *engaged* and *resetting* states, with a dramatic hinge-like swinging motion in the HSP101 hexamer accounting for the 20Å height difference. The TMD and B1–3 helices of EXP2 exhibit C7-symmetry, remaining identical between states (Supplementary Video 6). The deviation from C7-symmetry in the B4–5 helices and assembly domain is less pronounced in the *resetting* state (Extended Data Fig. 3b-c), likely due to the more planar arrangement of HSP101 protomers. As in the *engaged* state, slight inter-protomer variations in the PTEX150(S668-D823) H2–3 region bridge the gap between EXP2 and HSP101, maintaining a continuous protected path for unfolded cargo proteins.

The spiral staircase of HSP101 tyrosine pore loops in the *engaged* state collapses into a planar “C” shape in the *resetting* state (Supplementary Video 7), with a freedom of movement possibly conferred by the gap between HSP101 protomers 1 and 6[30,31]. Originating at the interface between the NBD2 domains of HSP101 protomers 3 and 4, HSP101 protomers 4–6 swing downwards and outwards, creating a deep vertical cleft through the central pore of the hexamer. This motion pulls the NBD2 loops in protomers 4–6 away from the unfolded cargo (Extended Data Fig. 3d-e,h-i, Supplementary Video 6–7). A shorter (19Å *vs* 45Å), unfolded cargo density remains visible, bound to the NBD2 loops in protomers 1–3, while no peptide density is visible in protomers 4–6 (Fig. 6a, Extended Data Fig. 3h-i). Furthermore, the NBD1 domain of protomer 3 rotates outward, such that the R361 arginine finger remains within 5.2Å of the ATPγS in the protomer 4 NBD1, while the nucleotide in the protomer 4 NBD2 shifts 7.5Å away from the R859 arginine finger in protomer 3 (Extended Data Fig. 3f-g).

Discussion

We propose a PTEX-mediated mechanism of protein translocation via a cyclic process involving at least two discrete states (Fig. 6b, Supplementary Video 6–7), which we have captured by purifying PTEX complexes directly from parasites actively translocating cargo. The pore loops in HSP101 NBD2 form two hands which work together to thread the cargo

protein through the central pore. NBD2 loops from HSP101 protomers 1–3 form the passive hand, located closest to the PTEX150(S668-D823)/EXP2 funnel, which stays fixed between states (Fig. 6a-b). NBD2 loops from HSP101 protomers 4–6 form the active hand, which moves along the channel axis (above the passive hand), grasping the unfolding peptide and feeding it through the passive hand. In the *engaged* state, all six NBD2 pore loops grip the unfolded peptide in the spiral staircase formation (Fig. 6a-b). As the HSP101 hexamer collapses into the *resetting* state, the active hand moves downwards, feeding the newly unfolded peptide through the passive hand, into the PTEX150(S668-D823)/EXP2 funnel below. The passive hand then grips the unfolded peptide, preventing it from slipping back toward the HSP101 apical entrance while the active hand swings outward, releasing the cargo (Fig. 6a-b). Finally, the active hand moves upwards to grasp the unfolding protein further upstream, transitioning back into the *engaged* state. With this elegant cyclic feeding mechanism, the unfolded cargo protein is threaded through the translocon, across the PVM and into the host cell cytosol.

The states captured here may be two of several states in the processive phase of translocation. Additional states likely exist for cargo-recognition. Although we did not observe PTEX-free HSP101 oligomers as suggested by Elsworth *et al.*[37], we did observe additional, seemingly cargo-free PTEX complexes (Extended Data Fig. 9) which did not refine to better than 7Å, suggesting conformational heterogeneity in the absence of stabilizing cargo interactions. Cargo-PTEX interactions during cargo-recognition may be transient, possibly explaining why we did not observe the HSP101 NTDs or other components potentially required for cargo-recognition. Without these details, the mechanisms for cargo-recognition and subsequent refolding after translocation remain unclear, although some evidence suggests involvement of exported parasite chaperones[38] or co-opted host chaperonins[39]. Interestingly, based on secondary structure prediction and PTEX150 truncation experiments[37], PTEX150 residues D838-F912 may occupy the claw (PTEX150 D838-E873) and three-turn helix (PTEX150 S884-F912) densities that remain unassigned in our structures.

Our work demonstrates the advantages of obtaining structures of challenging protein complexes in functionally relevant states by imaging samples purified directly from endogenous sources. Direct observation of the native PTEX core provides compelling evidence that this complex, comprising EXP2, PTEX150 and HSP101, is a *bona fide* translocon embedded in the PVM that serves as the gateway for the malaria parasite exportome. In addition to establishing the role of EXP2 as the membrane-spanning pore of PTEX and providing insight into the mechanism of this essential protein translocating machine, our structures reveal a unique interaction between the EXP2 assembly domain and the HSP101 C-terminal domain which is indispensable for PTEX function. These highly sought-after atomic structures of PTEX provide exciting possibilities for designing a new class of drugs inhibiting this essential gatekeeper of the malarial exportome.

Materials and Methods

Cells

P. falciparum strain NF54^{attB} [Ref 40] was used exclusively in the study. De-identified, IRB-exempt expired RBCs were obtained from the blood bank at the St. Louis Children's Hospital. PCR amplified regions from the NF54attB genome were found to match the genome sequence for 3D7, a sub clone of NF54. The prescence of the cg6 localized attB sequence was verified by successful Bxb1-mediated integration at that site.

Parasite culture and genetic modification for PTEX purification

P. falciparum culture was performed as described with the exception that RPMI was supplemented with 0.5% Albumax I [41]. All plasmid construction was carried out by Infusion cloning (Clontech) unless otherwise noted. Integration of a 3xFLAG fusion at the endogenous HSP101 C-terminus was accomplished with CRISPR/Cas9 editing. A Cas9 target site was chosen just upstream of the *hsp101* stop codon (TAATAGTAAAGCTAAAAACT) and the guide RNA seed sequence was synthesized as a sense and anti-sense primer pair (sense shown) 5'-TAAGTATATAATATTTAATAGTAAAGCTAAAAACTGTTTTAGAGCT

AGAA −3', annealed and inserted into the *BtgZI* site of the plasmid pAIO [42], resulting in the plasmid pAIO-HSP101-CT-gRNA1. A 5' homology flank (up to but not including the stop codon) was amplified from *P. falciparum* NF54^{attB} genomic DNA using primers 5'-GACGCGAGGAAAATTAGCATGCATCCTTAAGGAGATTCTGGTATGCCACTTGGTTC-3' and 5'- CTGCACCTGGCCTAGGGGTCTTAGATAAGTTTATAACTAAGTT TTTAGCTTTACTATT-3', incorporating a synonymous shield mutation in the protospacer adjustment motif of the gRNA target site within the *hsp101* coding sequence. A 3' homology flank (beginning 3 bp downstream of the stop codon) was amplified using primers 5'-CACTATAGAACTCGAGAATTACGCATATATATATATATATATATATATAACATGGGTTG-3' and 5'-GAACCAAGTGGCATACCAGAATCTCCTTAAGGATGCATGCTAATTTTCCTCGCGTC-3'F. The flank amplicons were assembled in a second PCR reaction using primers 5'-CACTATAGAACTCGAGAATTACGCATATATATATATATATATATATATAACATGGGTTG-3' and 5'-CTGCACCTGGCCTAGGGGTCTTAGATAAGTTTATAACTAAGTTTTTAGCTTTACTAT T-3' and inserted between *XhoI* and *AvrII* in pPM2GT[41]. The GFP tag between *AvrII* and *EagI* in this vector was then replaced with sequence encoding a 3xFLAG tag using the primer 5'-CTTAGTTATAAACTTATCTAAGACCCCTAGGGACTACAAGGACGACGACGACAAGG ATTATAAAGATGATGATGATAAAGATTATAAAGATGATGATGATAAATGACGGCCGC GTCGAGTTATATAATATATTTATG-3' and a QuikChange Lightning Multi Site-Directed Mutagenesis kit (Agilent), resulting in the plasmid pPM2GT-HSP101–3xFLAG. This plasmid was linearized at the *AflII* site between the 3' and 5' homology flanks and co-transfected with pAIO-HSP101-CT-gRNA1 into *P. falciparum* NF54^{attB} parasites[40]. Selection with 10 nM WR99210 was applied 24 hours after transfection. Once parasites

returned from selection, integration at the intended site was confirmed by PCR with primers 5'-CGAAAACTTTTATGGTATTAATATAACAG-3' and 5'-CCTTGTCGTCGTCGTCCTTG-3' and a clonal line was isolated by limiting dilution.

For PTEX purification, HSP101–3xFLAG parasites were synchronized by serial treatment with 5% w/v D-sorbitol and then expanded while shaking to increase singlet invasion events and maintain synchrony. For each preparation, ~2×10^{10} parasite-infected erythrocytes were collected at the ring stage (typically ~500 mls of 2% hematocrit culture at ~20% parasitemia). Erythrocytes were lysed in 10x pellet volume of cold phosphate buffered saline (PBS) containing 0.0125% saponin (Sigma, sapogenin content ≥10%) and EDTA-free protease inhibitory cocktail (Roche or Pierce). Released parasites were washed in cold PBS containing EDTA-free protease inhibitory cocktail and washed cell pellets were frozen in liquid nitrogen and stored at −80°C.

Affinity purification of PTEX core complex from parasite pellets

Frozen parasite pellets were resuspended in Lysis Buffer (25mM HEPES pH 7.4, 10mM $MgCl_2$, 150mM KCl, 10% Glycerol) and homogenized using a glass Dounce tissue homogenizer. The membrane fraction was isolated from the homogenized lysate by centrifugation at 100,000*g* for one hour. The membrane pellet was solubilized in Solubilization Buffer (25mM HEPES pH 7.4, 10mM $MgCl_2$, 150mM KCl, 10% Glycerol, 0.4% Triton X-100) and the solubilized membranes were then applied to anti-FLAG M2 Affinity Gel resin (Sigma). The resin was washed extensively in Wash Buffer (25mM HEPES pH 7.4, 10mM $MgCl_2$, 150mM KCl, 10% Glycerol, 0.015% Triton X-100), after which the protein was eluted from the affinity resin with Elution Buffer (25mM HEPES pH 7.4, 10mM $MgCl_2$, 150mM KCl, 2mM ATPγS, 0.015% Triton X-100, 500μg/ml FLAG peptide).

The presence and relative abundance of the three PTEX core components were verified by silver stained SDS-PAGE and tryptic digest liquid chromatography-mass spectrometry (Extended Data Fig. 1d-e). The extremely low yields achievable when purifying PTEX directly from *P. falciparum* parasites prohibited the conventional approach of evaluating sample quality by size exclusion chromatography. Thus, during the iterative process of screening for optimal purification conditions, sample quality was assessed by negative stain (uranyl acetate) transmission electron microscopy in an FEI TF20 microscope equipped with a TVIPS 16 mega-pixel CCD camera. Briefly, small datasets of ~100,000 particles were collected and 2D class averages were generated in RELION[43,44] to assess the presence of sufficient numbers of intact PTEX particles yielding "good" class averages exhibiting distinct features. For example, C7 symmetry could be recognized in top views, and the characteristic Clp/HSP100 layers were visible in side views (Extended Data Fig. 6a–c).

Cryo Electron Microscopy

3μl aliquots of purified PTEX core complex were applied to glow-discharged lacey carbon grids with a supporting ultrathin carbon film (Ted Pella). Grids were then blotted with filter paper and vitrified in liquid ethane using an FEI Vitrobot Mark IV or a home-made manual

plunger. CryoEM grids were screened in an FEI Tecnai TF20 transmission electron microscope while optimizing freezing conditions.

Higher resolution cryoEM images were collected on a Gatan K2-Summit direct electron detector in counting mode on an FEI Titan Krios at 300kV equipped with a Gatan Quantum energy filter set at a 20 eV slit width. Fifty frames were recorded for each movie at a pixel size of 1.04Å at the specimen scale, with a 200 ms exposure time and an average dose rate of 1.2 electrons per $Å^2$ per frame, resulting in a total dose of 60 electrons per $Å^2$ per movie. The final dataset consists of a total of 25,000 movies recorded in four separate sessions.

Image processing and 3D reconstruction

Frames in each movie were aligned, gain reference-corrected and dose-weighted to generate a micrograph using MotionCor2 [Ref [45]]. Aligned and un-dose-weighted micrographs were also generated and used for contrast transfer function (CTF) estimation using CTFFIND4 [Ref [46]] and PTEX particle picking by hand and using Gautomatch[47].

1,508,462 particles were extracted from 19,752 micrographs and initially binned by a factor of 2. After two rounds of reference-free two-dimensional (2D) classification in RELION, 422,713 particles were selected as “good” particles from distinct 2D class averages representing different views of the PTEX core complex. These particles were then used in a one-class *ab initio* reconstruction followed by homogeneous refinement in CryoSPARC[48], yielding a 4.8Å *ab initio* 3D map.

The original 422,713 “good” particles were then aligned in a 3D refinement in RELION using the 4.8Å CryoSPARC map as an initial reference. All subsequent image-processing steps were performed using RELION. After this refinement, the particles were unbinned, their centers recalculated and used to re-extract particles from the original micrographs without binning. The newly extracted, unbinned particles were then aligned with a second 3D refinement yielding a ~4.5Å reconstruction.

An exhaustive, iterative search of classification and refinement conditions was used to sort out different conformations and further improve resolution (Extended Data Fig. 9). Briefly, upon further sorting using 3D-classification without alignment, we identified two homogenous particle subsets corresponding to the *engaged* and *resetting* states (Extended Data Fig. 9). Particles in the two subsets were refined separately, yielding full maps with overall resolutions of 4.16Å and 4.23Å, respectively.

Focused 3D classification without alignment followed by focused refinement was used to further improve the resolution of mobile regions of the structure in both states. C7 symmetry was applied in the focused 3D classification and refinement steps of the heptameric halves, comprising EXP2 and PTEX150, yielding a 3.4Å *engaged* state map and a 3.5Å *resetting* state map (Extended Data Fig. 3,9). The same procedure, except with C1 symmetry, was applied to the hexameric half of the *engaged* state, yielding a 4.09Å map (Extended Data Fig. 3,9). This last step was also applied to the hexameric half of the *resetting* state, but did not yield improvements in resolution. Further efforts of focused 3D classification and refinement of individual HSP101 protomers, individual claws, and HSP101 N-terminal

domain densities in the two states did not ultimately yield improvements in resolution in either state.

Model Building and Refinement

Map interpretation was performed with UCSF Chimera[49] and COOT[50]. *P. falciparum* protein sequences were obtained from the National Center for Biotechnology Information (NCBI)[51] and the PlasmoDB[52] protein databases. PHYRE2 [Ref [53]] secondary structure predictions were used as an aid for initial manual sequence registration. Models for a single monomer of HSP101, PTEX150, and EXP2 in the *engaged* state were all built *de novo.* This first model for each protein monomer was then placed into the density maps of other protomers to aid de novo modeling of subsequent protomers. Individual protomers in the complex were then manually remodeled to ensure a close fit between densities and models. The same process was repeated for the *resetting* state. Manual refinement targeting protein geometry alone was done primarily along the periphery and flexible regions of the complex (*e.g.*, the MDs of HSP101). While their densities and backbone traces were visible, we were unable to model the claw with its connected three-turn helix, nor one of the 12 MD loops in the *resetting* state (Fig. 5g,h). The three-turn helix displayed a few bulky side chains interacting with the MD of HSP101, however the lack of backbone connection to our atomic model of the complex and the limited visibility of smaller side chains in this region have made sequence assignment challenging.

Manual refinement targeting both protein geometry and fit with the density map was used primarily in the core regions where resolution was higher and noise was minimal. Rotamers were fit manually in COOT and improved using the ‘Back-rub Rotamers’ setting. The resulting models for the complexes were subjected to the phenix.real_space_refine program in PHENIX[54]. Following this step, Molprobity[55] reported less than ideal clash scores and map-to-model cross-correlation. To improve the geometry and fit, manual adjustments were made to protein geometry and density map fit, with the additional step of using Molprobity[55] clash dots and sphere-refinement in COOT.

The complex was then broken into three portions: (1) symmetric regions of EXP2 and PTEX150, (2) HSP101, and (3) the full PTEX complex. These model segments were fed back to phenix.geometry_minimization in PHENIX and then to phenix.real_space_refine using simulated annealing and global minimization applying Emsley’s Ramachandran restraints[50]. Following another round of manual checks and improvements, all models were subjected to phenix.real_space_refine with default settings one last time.

All figures and videos were prepared with UCSF Chimera, Pymol[56], and Resmap[57]. Molprobity was used to validate the stereochemistry of the final models.

Genetic complementation

For expression of a complementing second copy of truncated EXP2, the *exp2* coding sequence up to codon position 221 was amplified with primers 5’-CGAATAAACACGATTTTTTCTCGAGATGAAAGTCAGTTATATATTT TCCTTTTTTTTGTTATTCTTCG-3’ and 5’-AATCAACTTTTGTTCGCTAGCTTTCTTTG ATTCCATAGATTTCAATTTCTCTTCC-3’ and inserted into the plasmid pyEOE-attP-

EXP2–3xMYC[20] between *XhoI* and *NheI*, resulting in the plasmid pyEOE-attP-EXP2Δ222–287-3xMYC. This plasmid was co-transfected with pINT[40] into EXP2^{apt}::HSP101–3xFLAG conditional knockdown parasites[20] at the mature schizont stage using a Nucleofector 2b and Basic Parasite Nucleofector kit 2 (Lonza). Selection with 2μM DSM1 [Ref [58]] was applied 24 h post transfection (in addition to 2.5 μg/ml Blasticidin S and 1 μM anhydrotetracycline (aTc) for maintenance of endogenous EXP2 translational control by the aptamer system) to facilitate integration into the attP site engineered in the benign *cg6* locus through integrase mediated attB x attP recombination. Following return from selection, parasites were cloned by limiting dilution, and expression of EXP2Δ222–287-3xMYC was confirmed by western blot.

Parasite growth assays

EXP2^{apt}::Δ222–287 parasites were extensively washed to remove aTc and plated with or without 1μM aTc in triplicate at an initial parasitemia of 1%. Media was changed every 48 h and 1:1 subculture was performed every other day beginning on day 4 to avoid culture overgrowth. Parasitemia (percent of total red blood cells (RBCs) infected) was measured every 24 h by flow cytometry on a FACSCanto (BD Biosciences) by nucleic acid staining of cultured RBCs with PBS containing 0.8 μg/ml acridine orange. Cumulative parasitemias were back calculated based on the subculture schedule and data were fit to an exponential growth equation to determine rate constants using Prism (Graphpad).

Quantification of protein export

For evaluation of protein export by immunofluorescence assay (IFA), mature schizonts were purified on a magnetic column and allowed to invade fresh, uninfected RBCs with shaking for 3 hours before treatment with 5% w/v D-sorbitol to destroy unruptured schizonts. Pulse invaded cells were plated with or without 1 μM aTc and allowed to develop 24 h post invasion. Thin smears of infected RBCs were briefly air dried and immediately fixed in ice cold acetone for 2 minutes. After fixation, samples were blocked for 30 minutes in PBS+3% BSA followed by incubation for one hour with primary antibody solutions containing mouse anti-FLAG M2 mAb (detecting HSP101–3xFLAG to mark the PVM) and rabbit anti-SBP1. After washing, secondary antibody incubation was carried out for one hour with Alexa Fluor anti-mouse 488 and anti-rabbit 594 IgG antibodies (Life Technologies), each diluted 1:2000. After final washing, coverslips were mounted over each sample using Pro-long antifade Gold with DAPI (Life Technologies). Images were collected with an ORCA-ER CCD camera (Hamamatsu) using AxioVision software on an Axio Imager.M1 microscope (Zeiss) with a 100x oil immersion objective using the same exposure times for each image (300 ms for SBP1–594, 150 ms for FLAG-488). Ten images were acquired for each condition using the DAPI channel for field selection to avoid bias. Images were then analyzed using Volocity 6.3 (PerkinElmer). The border of each single-infected erythrocyte was traced using the DIC channel as a guide to define a region of interest (ROI). The PVM was marked using the “find objects” measurement tool for the HSP101–3xFLAG-488 channel (automatic threshold setting with threshold offset set to −30% and minimum object size set to 0.5 μm^2). Individual Maurer’s clefts were identified using the “find spots” measurement tool for the SBP1–594 channel (offset minimum spot intensity set to 40% and brightest spot within radius set to 0.5 μm). All spots within the PVM object boundary were then removed using

the “subtract” measurement tool and the number and fluorescent intensity of the remaining spots in each ROI were collected. Data were pooled from two independent experiments and plotted with Prism.

Antibodies

The following primary antibodies were used for IFA and western blot: mouse anti-FLAG mAb clone M2 (Sigma) (IFA: 1:500, WB 1:500); rabbit polyclonal anti-SBP1 [Ref 59] (IFA: 1:500); mouse anti-cMYC mAb 9E10 (ThermoFisher) (WB: 1:300).

Extended Data

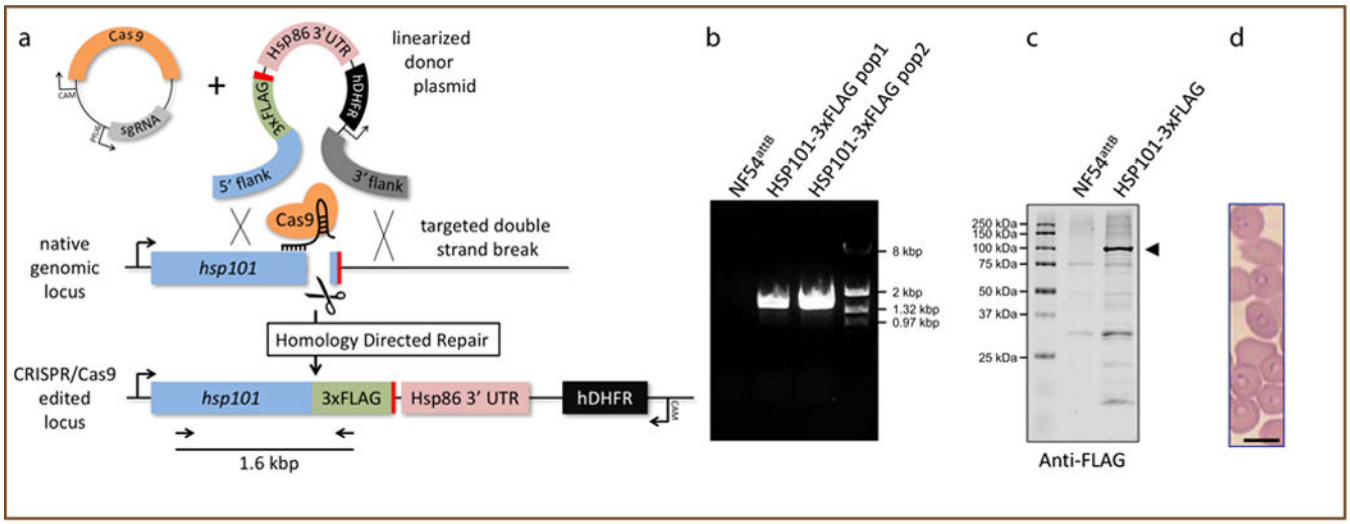

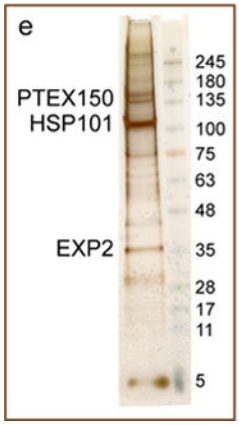

f

	Accession	Seq coverage	Seq count	Spec count	NSAF	EMPAI	Description
1	PF3D7_1116800	55.5	72	228	0.0750967	2.5892193	product=heat shock protein 101 (HSP101)
2	PF3D7_0917900	48.3	44	101	0.04622617	2.040885	product=heat shock protein 70 (HSP70-2)
3	PF3D7_1436300	58	58	135	0.04056941	2.8018937	product=translocon component PTEX150 (PTEX150)
4	PF3D7_1471100	40.8	13	34	0.03535177	1.5585859	product=exported protein 2 (EXP2)
5	PF3D7_1006200	59.8	7	7	0.019522185	2.9627802	product=DNA/RNA-binding protein Alba 3 (ALBA3)

Extended Data Figure 1. Generation of HSP101–3xFLAG parasites and analysis of purified PTEX .

a, Schematic showing strategy for endogenous tagging of *P. falciparum hsp101* with 3xFLAG using CRISPR/Cas9 editing. Diagnostic PCR primers and expected amplicon following successful integration are shown. sgRNA, single guide RNA; UTR, untranslated region; CAM, calmodulin promoter; PfU6, *P. falciparum* U6 promoter; hDHFR, human dihydrofolate reductase. **b**, Diagnostic PCR with genomic DNA template from NF54^{attB} parent or two independent populations of HSP101–3xFLAG parasites. kb, kilobase pairs. The experiment was performed one time. **c**, Western blot of NF54^{attB} and HSP101–3xFLAG parasites probed with mouse-anti-FLAG M2 antibody (Sigma) and goat-anti-mouse IRDye 680 secondary (Li-cor). Arrowhead indicates full-length HSP101–3xFLAG (predicted molecular weight 102.9 kDa after signal peptide cleavage). kDa, kilodaltons. Data represent two independent experiments. **d**, Giemsa staining of parasite-infected human erythrocytes from which PTEX was purified. Scale bar: 5um. For source data, see Supplementary Figure 3. **e**, Silver stained SDS-PAGE gel of the FLAG-purified PTEX sample. Identities of the bands labeled EXP2, PTEX150, and HSP101 were confirmed by tryptic digest LC-MS. **f**, Tryptic digest liquid chromatography-mass spectrometry (LC-MS) analysis of the FLAG-purified PTEX sample. The PTEX core components are among the five most abundant

species detected in the purified sample. For gel and blot source data, see Supplementary Figure 1.

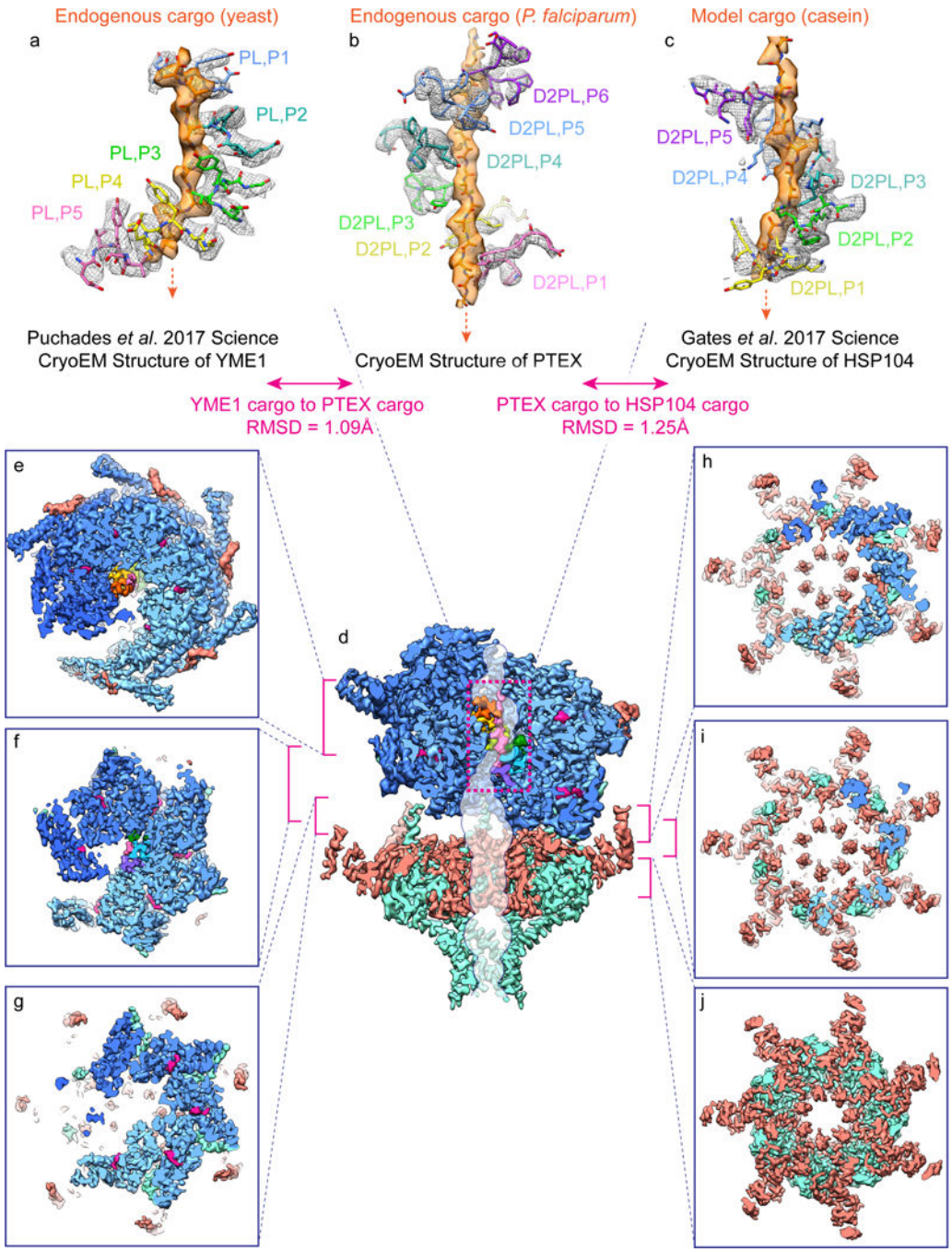

Extended Data Figure 2. Detailed views of the PTEX protein-conducting channel and symmetry mismatch in the *engaged* state.

CryoEM densities and atomic models of cargo and pore loops from the near-atomic resolution structures of Clp/HSP100 ATPases YME1[61] (**a**), PTEX HSP101 (**b**), and HSP104[31] (**c**). Tyrosine sidechain densities are clearly visible intercalating with the cargo densities. The modeled *engaged* state PTEX cargo has a calculated RMSD of 1.09Å and 1.25Å to the published YME1 and HSP104 cargo models, respectively. Pore loops are labeled by NBD and protomer (e. g., D2PL,P1: NBD2 Pore Loop, Protomer 1). **d**, Side view

of the bisected *engaged* state PTEX cryoEM map. The protein-conducting channel, calculated using HOLE[60], is shown superimposed over the bisected map in translucent white with a navy outline. The HSP101 NBD2 pore loop densities are colored by HSP101 protomer, and the cargo density is colored pink. **e-j**, The transition from the assymetric HSP101 spiral to the C7 pseudosymmetric PTEX150(668–823)-EXP2 heptamer is depicted using a series of cross sections taken perpendicular to the central axis of the translocon, spanning the area of symmetry mismatch. The section of the translocon corresponding to each cross-sectional image is indicated with a brackets in (**d**).

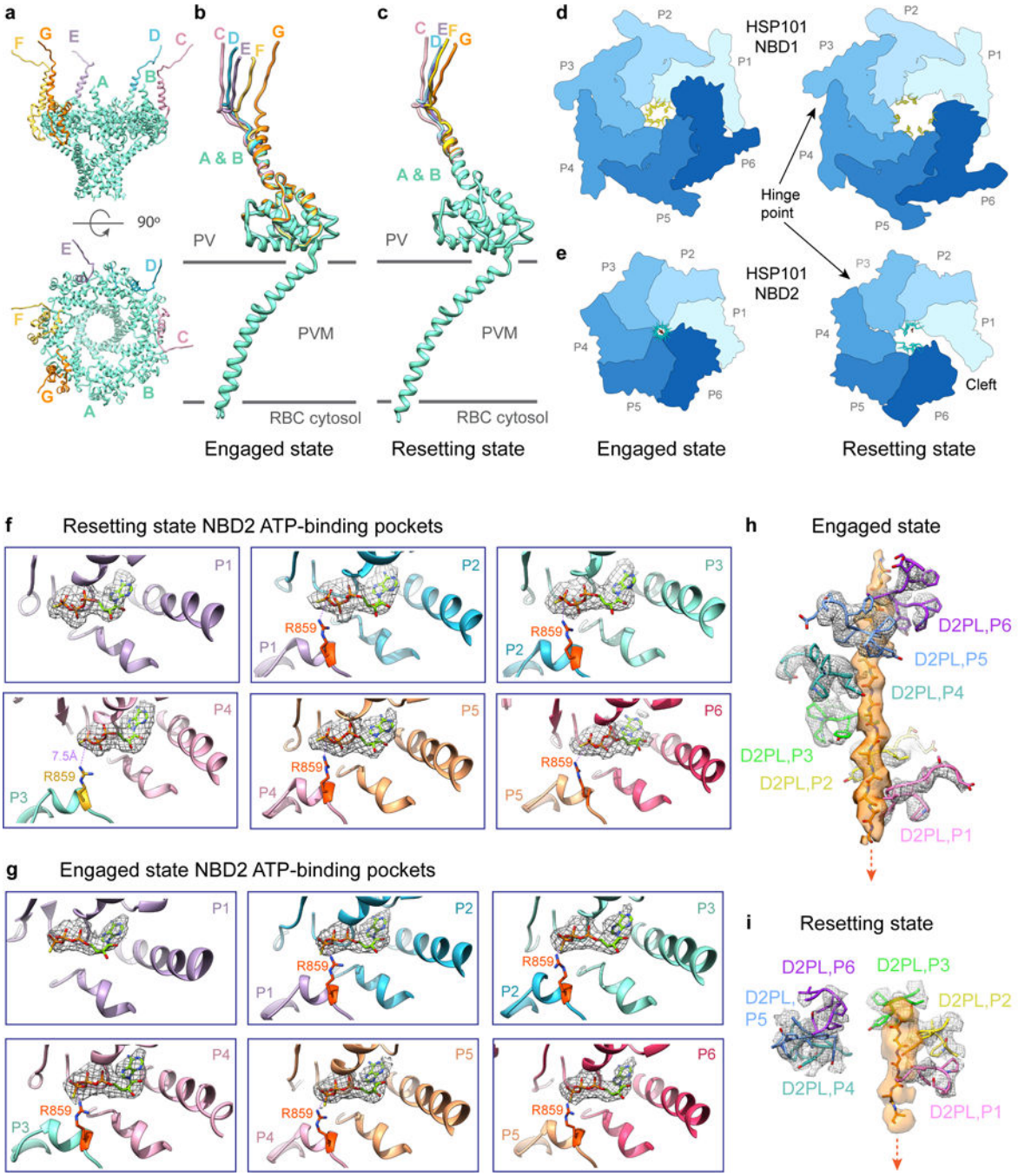

Extended Data Figure 3. Detailed comparisons of the *engaged* and *resetting* states.

a, Side and top views of the EXP2 heptamer in the *engaged* state. Symmetric portions that remain constant between protomers are colored in mint. Portions that vary between protomers are colored and labeled by protomer. **b-c**, Superposition of the seven EXP2 protomers, labeled A-G, in the *engaged* (**b**) and *resetting* (**c**) states, colored as in (**a**). Ribbon diagrams of the *resetting* state (**a**) and *engaged* state (**b**) nucleotide binding pockets are shown for each protomer. **d-e**, Top view of HSP101 NBD1 (**d**) and NBD2 (**e**) in the *engaged* and *resetting* states, shown in simplified surface representation. The hinge point at the

interface between HSP101 protomers 3 and 4 is indicated. **f-g**, Ribbon diagrams of the *resetting* state (**f**) and *engaged* state (**g**) nucleotide binding pockets are shown for each protomer. ATPγS in each pocket is shown with corresponding cryoEM density (mesh). The R859 arginine finger (sidechain shown in red-orange) is positioned ~3–5.5Å from the phosphorous atom in the γ-phosphate of the ATPγS in the binding pocket of the neighboring protomer in all protomers except R859 in protomer 3 in the *resetting* state (sidechain shown in gold), where the ATPγS bound in the protomer 4 NBD2 nucleotide pocket has shifted ~7.5Å away from the protomer 3 R859 arginine finger. **h-i**, Enlarged side view of the atomic models of the HSP101 NBD2 pore loops and unfolded cargo polypeptide backbone in the *engaged* (**h**) and *resetting* (**i**) states, shown with corresponding cryoEM densities. Tyrosine sidechain densities are clearly visible intercalating with the cargo densities. The modeled PTEX cargo has a calculated RMSD of 1.09Å and 1.25Å to the published YME1 and HSP104 cargo models, respectively. Pore loops are labeled by NBD and protomer (e. g., D2PL,P1: NBD2 Pore Loop, Protomer 1).

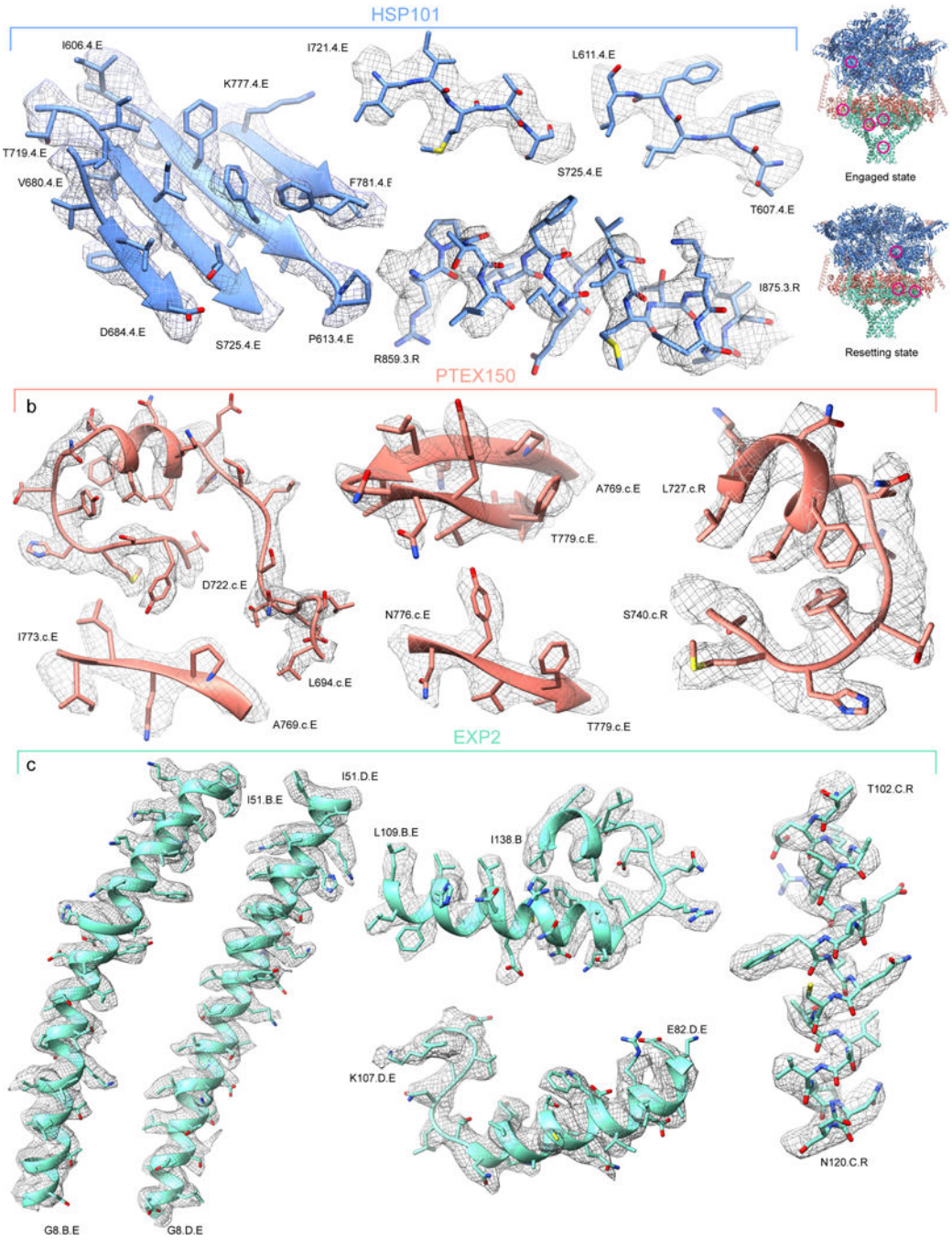

Extended Data Figure 4. Resolution assessments of the two PTEX states.

a-c,e-f Local resolution evaluations of the full PTEX map (**a**) and the focus-refined maps of the upper/hexameric (**b**) and lower/heptameric (**c**) halves of PTEX in the *engaged* state, and the full PTEX map (**e**) and the focus-refined map of the lower/heptameric (**f**) half of PTEX in the *resetting* state, calculated by Resmap[57] and colored according to resolution. Maps are displayed at higher thresholds where the detergent belt is not visible for clarity, to avoid obscuring details of the transmembrane helices. **d**, Global resolution assessment of the *engaged* and *resetting* state maps as measured using the "Gold-standard" Fourier shell

correlation (FSC) curves generated by RELION[43,44] by comparison of two independently refined “half-maps”. **g**, Map-to-model FSC curves demonstrating the degree of correlation between the refined PTEX models and the experimental cryoEM maps for the *engaged* and *resetting* states.

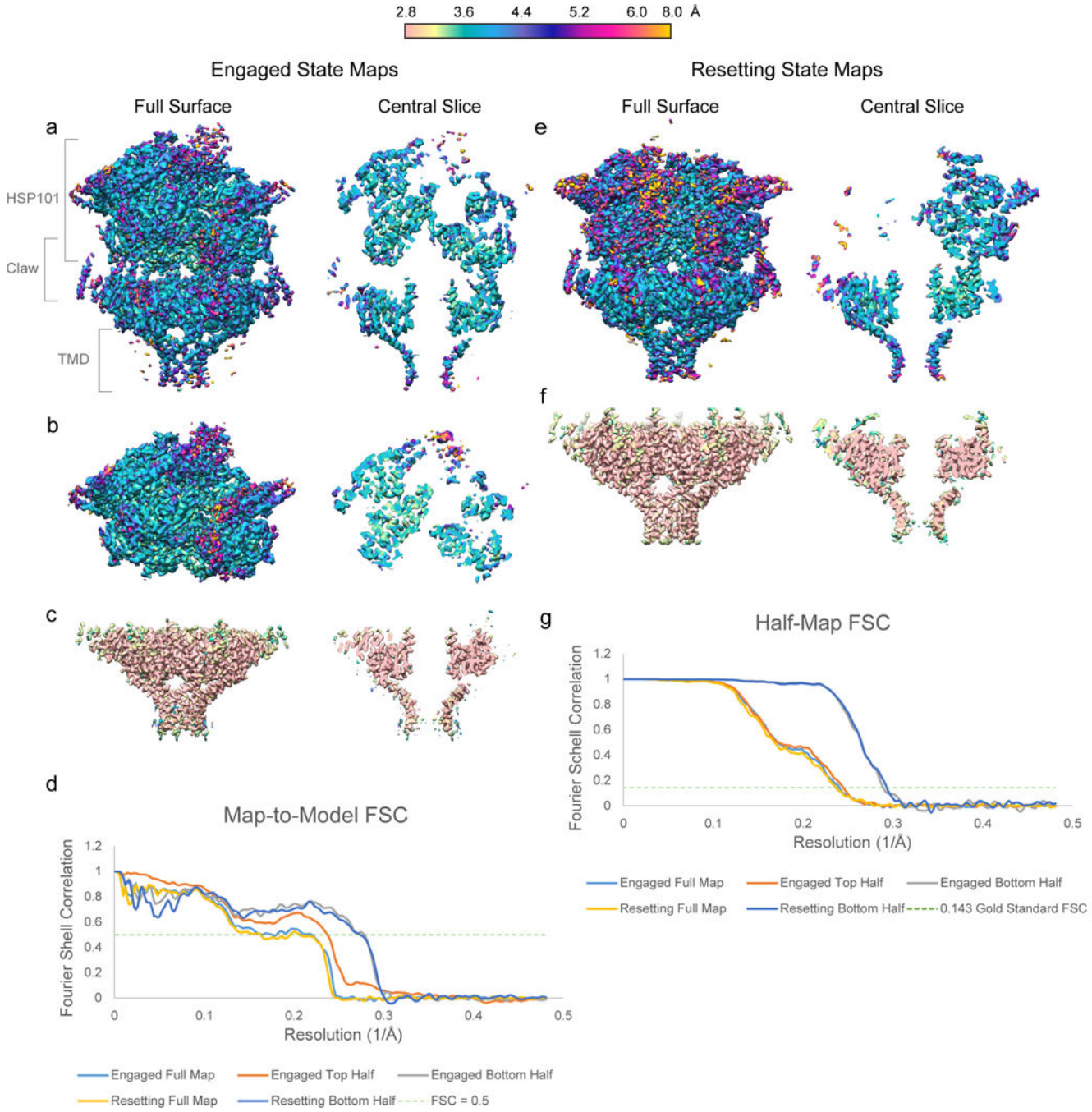

Extended Data Figure 5. Representative regions of cryoEM density and atomic models.

Additional cryoEM densities (mesh) superposed with our atomic models for HSP101 (**a**), PTEX150(668–823) (**b**), and EXP2 (**c**). Displayed regions correspond to areas circled in magenta on guide figures (inset, upper right), and are colored as in guide figure: HSP101 (cornflower blue), PTEX150(668–823) (salmon), EXP2 (mint). Terminal residues for each segment are labeled with the amino acid, residue number, protomer, and state.

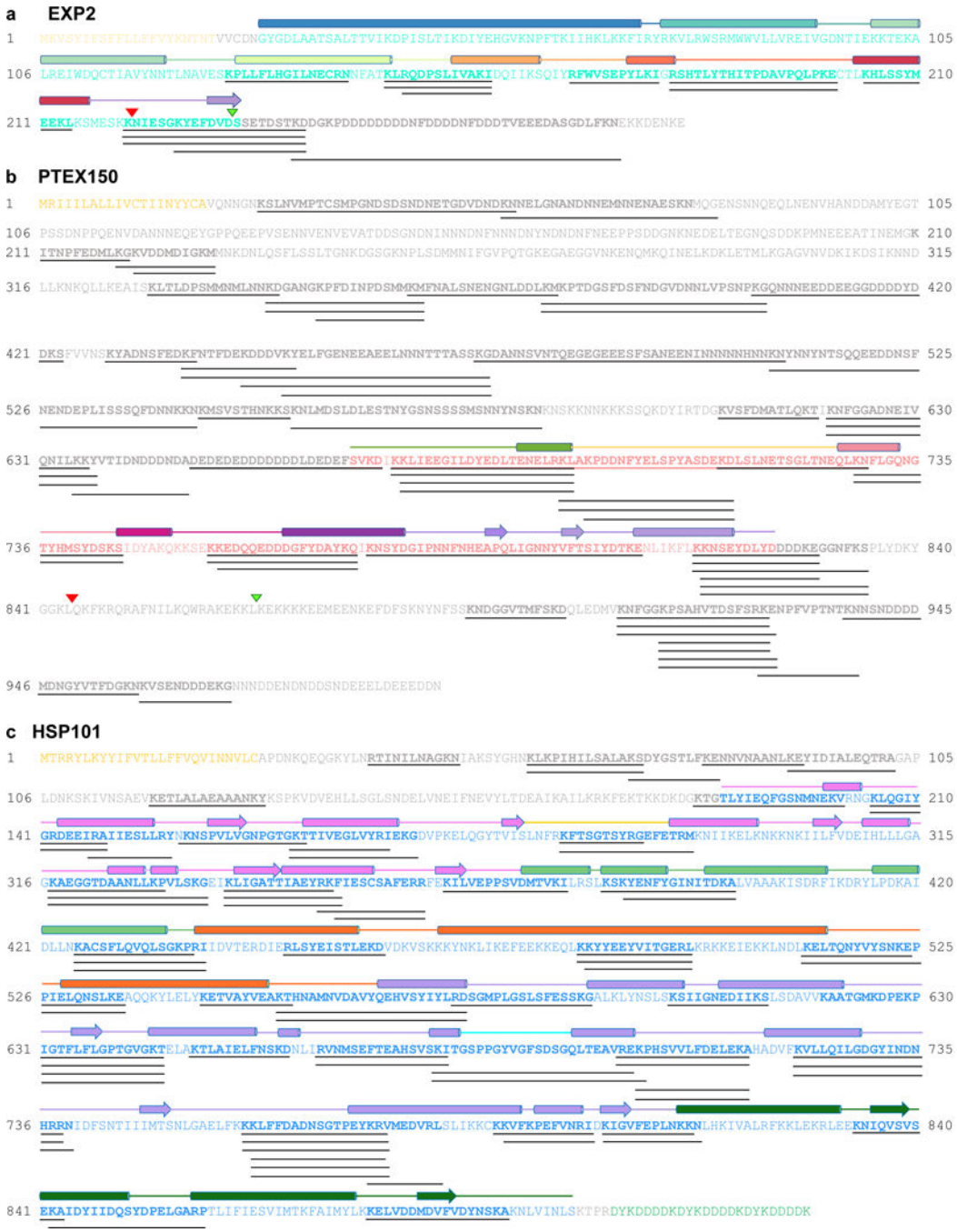

Extended Data Figure 6. Experimentally determined secondary structure elements and detected mass-spec fragments mapped to the primary sequences of the three PTEX proteins.

For EXP2 (**a**), PTEX150 (**b**), and HSP101 (**c**), secondary structure elements are shown as tubes (helices), lines (loops), and arrows (strands) above the corresponding sequence and are colored as in Fig. 2a, 3a, and 4a. In the sequences shown below, residues resolved in our structures are colored according to protein colors in Fig. 1c–f: EXP2 (mint), PTEX150 (salmon) and HSP101 (cornflower). Signal peptide residues are colored gold. All residues in the mature proteins that are not resolved in our structures are shown in grey. The 3xFLAG residues at the C-terminus of HSP101 are colored green. Peptides detected in tryptic digest

LC-MS/MS analysis of the purified PTEX sample are shown as black lines below the corresponding sequences. Arrowheads above the EXP2 sequence indicate truncations sites described in this work and in Garten *et al.*[20] immediately before (Δ222–287, red arrowhead) and after (Δ234–287, green arrowhead) the assembly strand. Arrowheads above PTEX150 sequence indicate previously described truncation sites[37] (Δ847–993, red arrowhead; Δ869–993, green arrowhead).

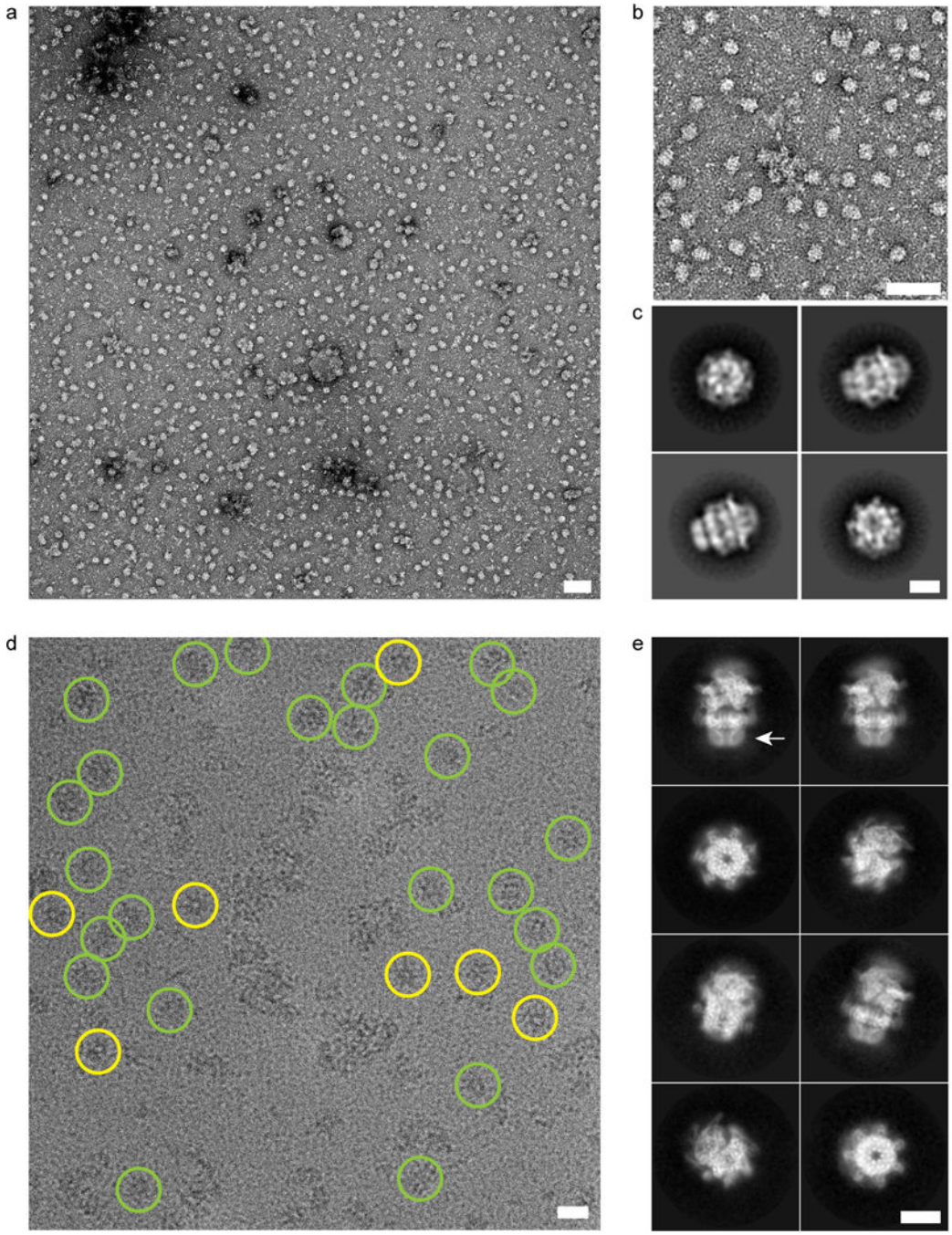

Extended Data Figure 7. EM of the PTEX core complex.

a-c Representative negative stain micrograph (**a**), enlarged portion of micrograph (**b**), and two-dimensional class averages (**c**) of the PTEX core complex in multiple orientations. **d,e** Representative cryoEM micrograph (**d**) and two-dimensional class averages (**e**) of the PTEX core complex in multiple orientations. Arrow in upper left panel of (**e**) indicates the detergent belt, which is visible as a less-dense (dimmer) halo surrounding the denser (brighter) densities of the alpha helices visible in the TMD in side views. Scale bars are 700Å, 700Å, 100Å, 200Å and 100Å, respectively.

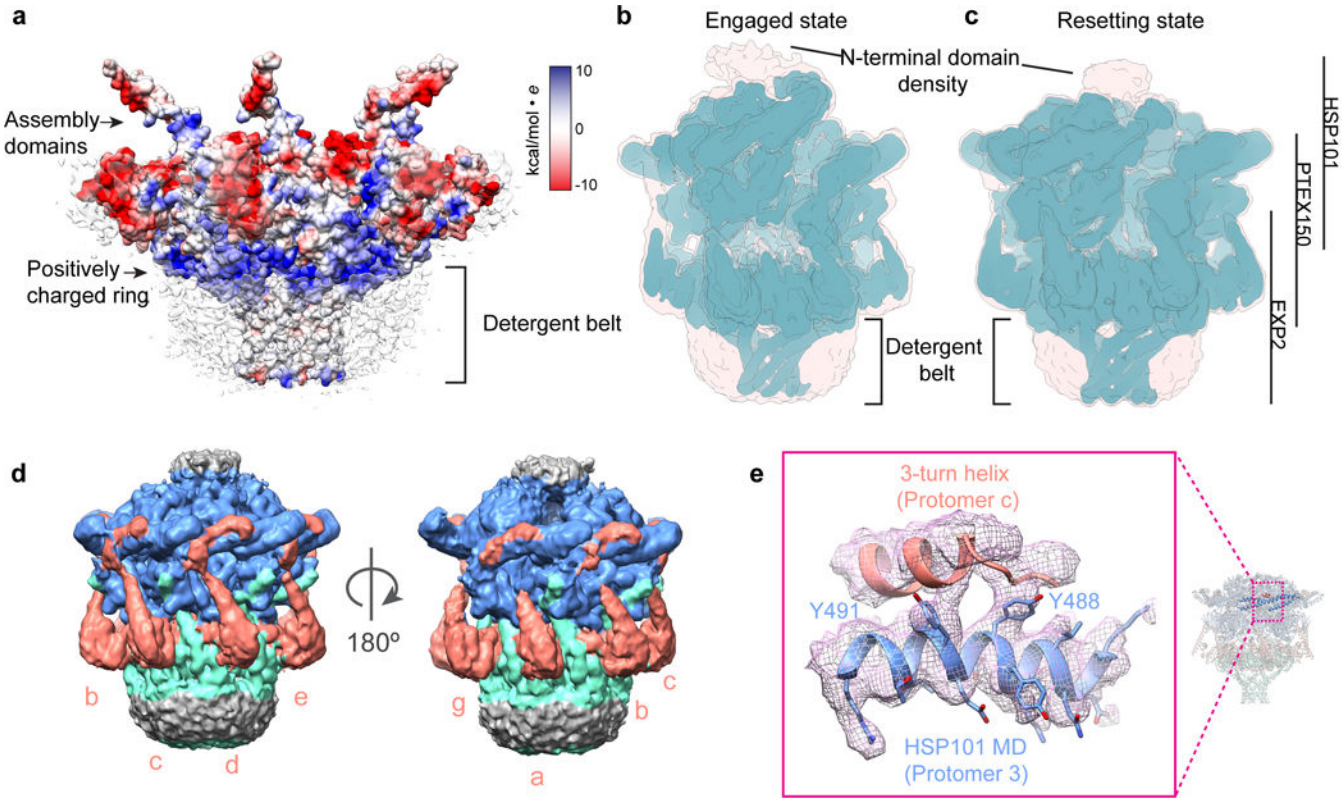

Extended Data Figure 8. Detergent belt, amino-terminal domain, and claw densities visible in maps at lower thresholds.

a, The *engaged* state PTEX150/EXP2 heptamer, displayed in surface representation and colored by electrostatic potential. The bottom half of the full *engaged* state density map is superimposed, showing the location of the detergent belt in relation with the EXP2 TMD. A ring of positively charged residues is clearly visible directly above where the PVM surface would normally lie. **b,c** *Engaged* state (**b**) and *resetting* state (**c**) maps were low-pass filtered to 6Å to improve clarity of low resolution details, and are shown overlaid, at two different thresholds to improve visibility of the detergent belt and the poorly-resolved N-terminal domains of HSP101 (teal, higher threshold; peach, lower threshold). **d**, *Resetting* state map of PTEX displayed at a lower threshold to show the strong claw-shaped densities extending from the PTEX150(668–823) shaft up to the HSP101 MD. **e**, Enlarged view of the interaction between HSP101 Y488 and Y491 and the three-turn helix, shown with corresponding cryoEM density (mesh).

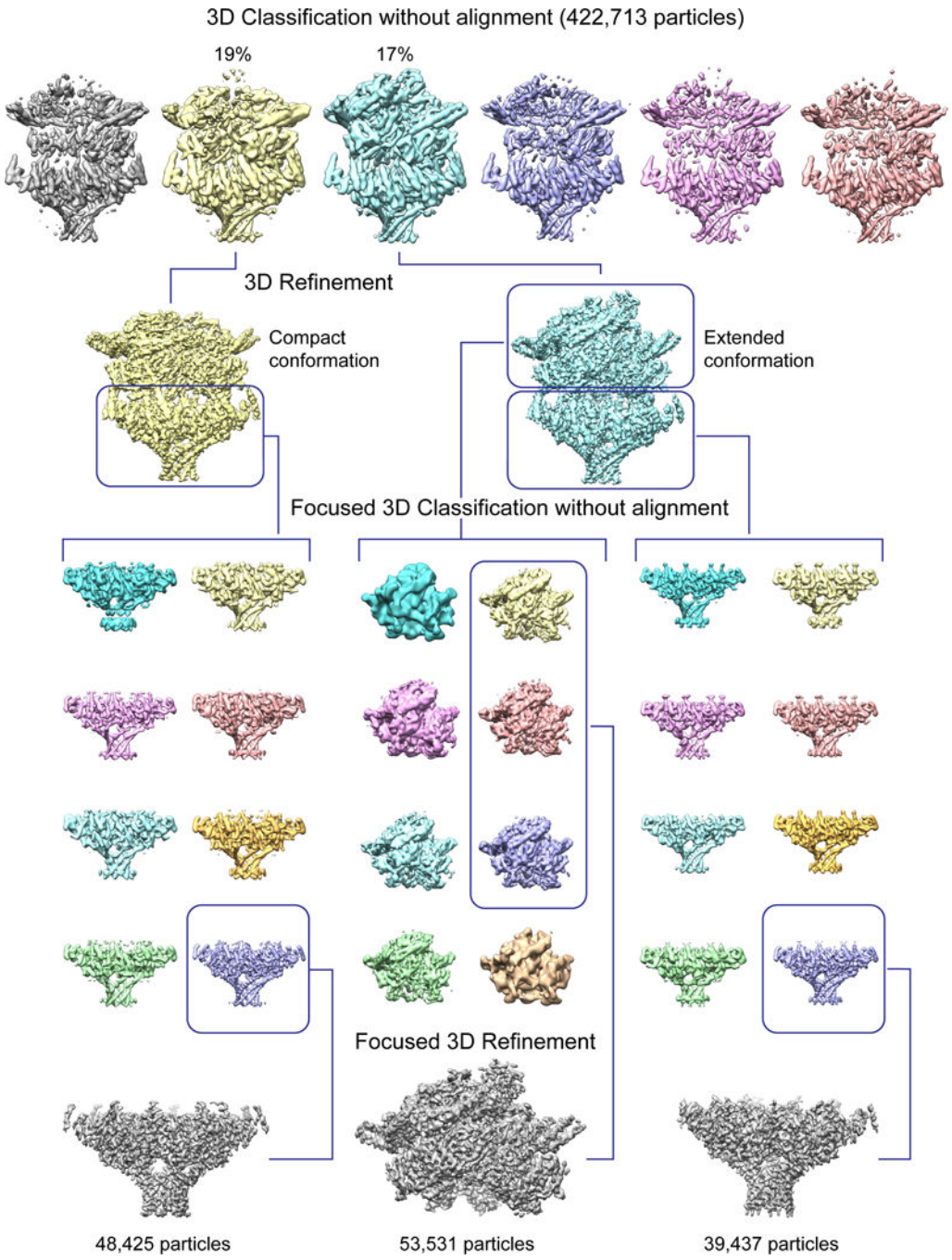

Extended Data Figure 9. Data processing workflow.

Illustration of workflow for 3D classification, and focused classification and refinement. Maps are displayed at higher thresholds where the detergent belt is not visible for clarity, to avoid obscuring details of the transmembrane helices.

Extended Data Table 1

Cryo-EM data collection, refinement and validation statistics.

	PTEX *Engaged* Full (EMDB-8951) (PDB 6E10)	**PTEX *Engaged* Top (EMDB-8951) (PDB 6E10)**	**PTEX *Engaged* BoCoen (EMDB-8951) (PDB 6EI0)**	**PTEX *Resetting* Fun (EMDB-8952) (PDB 6E11)**	**PTEX *Resetting* Top (EMDB-8952) (PDB 6E11)**	**PTEX *Resetting* Bottom (EMDB-8952) (PDB 6E11)**
Data collection and processing						
Magnification	×**105,000**	×**105,000**	×**105,000**	×**105,000**	**n/a**	×**105,000**
Voltage (kV)	300	300	300	300	n/a	300
Electron exposure (e-/Å^2)	60	60	60	60	n/a	60
Defocus range (μm)	−1 5 to – 40	−1 5 to – 40	−1 5 to – 40	−1 5 to – 40	n/a	−1 5 to – 40
Pixel size (Å)	1.04	1.04	1.04	1 04	n/a	1.04
Symmetry nrcanl	Cl	Cl	C7	Cl	n/a	C7
Initial particle traces (no)	**1,508,462**	**1,508,462**	**1,508,462**	**1,508,462**	**n/a**	**1,508,462**
Final purticle images (no)	**72,966**	**53,531**	**39,437**	**78,499**	**n/a**	**48,425**
Map resolution (Å) FSC threshold	4.09 0.143	4 16 0.143	3.5 0.143	4.23 0.143	n/a	3.4 0.143
Map resolution range (Å)	3.2–7.5	3.0–7.0	2.8–3.6	3.2–7.5	n/a	2. 8–3.4
Refinement						
Initial model wed (PDB cock)	n/a	n/a	n/a	n/a	n/a	n/a
Model resolution (Å) FSC threshold	4.58 0.5	4.23 0.5	3.59 0.5	4.84 0.5	n/a	3.67 0.5
Model resoluion range (Å)	4.58	4.23	3.59	4.84	n/a	3.67
Map sharpening *B* factor (Å^2)	−180	−180	−170	−180	n/a	−160
Model compoution Non-hydrogen atoms Protein residues Legand	57,352 6,838 12	57,352 6,838 12	57,352 6,838 12	57,401 6,826 12	57,401 6,826 12	57,401 6,826 12
B factor (Å^2) Protein Legand	n/a	n/a	n/a	n/a	n/a	n/a
R.m.s. deviation Bond lengths (Å) Bond angles (°)	0.008 1.311	0.009 1.262	0.008 0.925	0.008 1.300	0.007 1.332	0.006 0.895
Validation MolProhety score (Clashscore Poor rotamers(%)	1.95 9.74 1.04	1.81 7.35 0.13	1.53 4.01 0.45	2.03 10.44 0.47	1.96 7.46 0.05	1.64 5.48 0.33
Ramachandran plot Favored (%) Allowed (%) Disallolwed (%)	93.96 5.53 0 51	94.01 5.76 0.23	94.99 4.69 0.33	91.91 7.65 0.44	89.98 9.58 0.44	94.98 5.01 0.00

Supplementary Material

Refer to Web version on PubMed Central for supplementary material.

Acknowledgements

This research was supported in part by grants from National Institutes of Health (R21AI125983 to P.F.E., R01GM071940/AI094386/DE025567 to Z.H.Z. and K99/R00 HL133453 to J.R.B.). P.F.E. is the Alexander and Renee Kolin Endowed Chair in Molecular Biology and Biophysics. CM.H. acknowledges funding from the Ruth L. Kirschstein National Research Service Award (AI007323). We thank the UCLA Proteome Research Center for assistance in mass spectrometry and acknowledge the use of instruments in the Electron Imaging Center for Nanomachines supported by UCLA and grants from NIH (S10RR23057, S10OD018111 and U24GM116792) and NSF (DBI-1338135 and DMR-1548924). We thank Anthony W. P. Fitzpatrick for input on cryoEM aspects of the project and Judy Su for helping with Figure 1a.

References

1. WHO. World malaria report 2017. Report No. ISBN: 978 92 4 156552 3, 196 (2017).
2. Miller LH, Ackerman HC, Su XZ & Wellems TE Malaria biology and disease pathogenesis: insights for new treatments. Nat Med 19, 156–167, 10.1038/nm.3073 (2013). [PubMed: 23389616]
3. Cowman AF, Healer J, Marapana D & Marsh K Malaria: Biology and Disease. Cell 167, 610–624, 10.1016/j.cell.2016.07.055 (2016). [PubMed: 27768886]
4. Spillman NJ, Beck JR & Goldberg DE Protein Export into Malaria Parasite-Infected Erythrocytes: Mechanisms and Functional Consequences. Annu Rev Biochem 84, 813–841, 10.1146/annurev-biochem-060614-034157 (2015). [PubMed: 25621510]
5. Boddey JA & Cowman AF Plasmodium Nesting: Remaking the Erythrocyte from the Inside Out. Annu Rev Microbiol 67, 243–269, 10.1146/annurev-micro-092412-155730 (2013). [PubMed: 23808341]
6. Przyborski JM, Nyboer B & Lanzer M Ticket to ride: export of proteins to the Plasmodium falciparum-infected erythrocyte. Mol Microbiol 101, 1–11, 10.1111/mmi.13380 (2016). [PubMed: 26996123]
7. de Koning-Ward TF, Dixon MW, Tilley L & Gilson PR Plasmodium species: master renovators of their host cells. Nat Rev Microbiol 14, 494–507, 10.1038/nrmicro.2016.79 (2016). [PubMed: 27374802]
8. Marti M, Good RT, Rug M, Knuepfer E & Cowman AF Targeting malaria virulence and remodeling proteins to the host erythrocyte. Science 306, 1930–1933, 10.1126/science.1102452 (2004). [PubMed: 15591202]
9. Hiller NL et al. A host-targeting signal in virulence proteins reveals a secretome in malarial infection. Science 306, 1934–1937, 10.1126/science.1102737 (2004). [PubMed: 15591203]
10. Heiber A et al. Identification of new PNEPs indicates a substantial non-PEXEL exportome and underpins common features in Plasmodium falciparum protein export. PLoS Pathog 9, e1003546, 10.1371/journal.ppat.1003546 (2013). [PubMed: 23950716]
11. Lingelbach K & Joiner KA The parasitophorous vacuole membrane surrounding Plasmodium and Toxoplasma: An unusual compartment in infected cells. J Cell Sci 111, 1467–1475 (1998). [PubMed: 9580555]
12. Ansorge I, Benting J, Bhakdi S & Lingelbach K Protein sorting in Plasmodium falciparum-infected red blood cells permeabilized with the pore-forming protein streptolysin O. Biochem J 315, 307–314, 10.1042/bj3150307 (1996). [PubMed: 8670123]
13. Gehde N et al. Protein unfolding is an essential requirement for transport across the parasitophorous vacuolar membrane of Plasmodium falciparum. Mol Microbiol 71, 613–628, 10.1111/j.1365-2958.2008.06552.x (2009). [PubMed: 19040635]
14. de Koning-Ward TF et al. A newly discovered protein export machine in malaria parasites. Nature 459, 945–949, 10.1038/nature08104 (2009). [PubMed: 19536257]

15. Beck JR, Muralidharan V, Oksman A & Goldberg DE PTEX component HSP101 mediates export of diverse malaria effectors into host erythrocytes. Nature 511, 592–595, 10.1038/nature13574 (2014). [PubMed: 25043010]
16. Elsworth B et al. PTEX is an essential nexus for protein export in malaria parasites. Nature 511, 587-+, 10.1038/nature13555 (2014). [PubMed: 25043043]
17. Bullen HE et al. Biosynthesis, Localization, and Macromolecular Arrangement of the Plasmodium falciparum Translocon of Exported Proteins (PTEX). J Biol Chem 287, 7871–7884, 10.1074/jbc.M111.328591 (2012). [PubMed: 22253438]
18. Johnson D et al. Characterization of Membrane-Proteins Exported from Plasmodium-Falciparum into the Host Erythrocyte. Parasitology 109, 1–9, 10.1017/S0031182000077696 (1994). [PubMed: 8058359]
19. Gold DA et al. The Toxoplasma Dense Granule Proteins GRA17 and GRA23 Mediate the Movement of Small Molecules between the Host and the Parasitophorous Vacuole. Cell Host Microbe 17, 642–652, 10.1016/j.chom.2015.04.003 (2015). [PubMed: 25974303]
20. Garten MN,AS; Niles JC; Zimmerberg J; Goldberg DE; Beck JR . EXP2: a dual function channel protein in the malaria parasite vacuolar membrane. Nature Microbiology
21. Chisholm SA et al. The malaria PTEX component PTEX88 interacts most closely with HSP101 at the host-parasite interface. FEBS J, 10.1111/febs.14463 (2018).
22. Holm L & Laakso LM Dali server update. Nucleic Acids Res 44, W351–355, 10.1093/nar/gkw357 (2016). [PubMed: 27131377]
23. Gibrat JF, Madej T & Bryant SH Surprising similarities in structure comparison. Curr Opin Struct Biol 6, 377–385 (1996). [PubMed: 8804824]
24. Wiederstein M, Gruber M, Frank K, Melo F & Sippl MJ Structure-based characterization of multiprotein complexes. Structure 22, 1063–1070, 10.1016/j.str.2014.05.005 (2014). [PubMed: 24954616]
25. Krissinel E & Henrick K Secondary-structure matching (SSM), a new tool for fast protein structure alignment in three dimensions. Acta Crystallogr D 60, 2256–2268, 10.1107/S0907444904026460 (2004). [PubMed: 15572779]
26. Dosztanyi Z, Csizmok V, Tompa P & Simon I IUPred: web server for the prediction of intrinsically unstructured regions of proteins based on estimated energy content. Bioinformatics 21, 3433–3434, 10.1093/bioinformatics/bti541 (2005). [PubMed: 15955779]
27. Dosztanyi Z, Csizmok V, Tompa P & Simon I The pairwise energy content estimated from amino acid composition discriminates between folded and intrinsically unstructured proteins. J Mol Biol 347, 827–839, 10.1016/j.jmb.2005.01.071 (2005). [PubMed: 15769473]
28. Schirmer EC, Glover JR, Singer MA & Lindquist S HSP100/Clp proteins: A common mechanism explains diverse functions. Trends Biochem Sci 21, 289–296, 10.1016/S0968-0004(96)10038-4 (1996). [PubMed: 8772382]
29. Hanson PI & Whiteheart SW AAA+ proteins: have engine, will work. Nat Rev Mol Cell Biol 6, 519–529, 10.1038/nrm1684 (2005). [PubMed: 16072036]
30. Deville C et al. Structural pathway of regulated substrate transfer and threading through an Hsp100 disaggregase. Sci Adv 3, e1701726, 10.1126/sciadv.1701726 (2017). [PubMed: 28798962]
31. Gates SN et al. Ratchet-like polypeptide translocation mechanism of the AAA+ disaggregase Hsp104. Science 357, 273–279, 10.1126/science.aan1052 (2017). [PubMed: 28619716]
32. AhYoung AP, Koehl A, Cascio D & Egea PF Structural mapping of the ClpB ATPases of Plasmodium falciparum: Targeting protein folding and secretion for antimalarial drug design. Protein Sci 24, 1508–1520, 10.1002/pro.2739 (2015). [PubMed: 26130467]
33. Puchades C et al. Structure of the mitochondrial inner membrane AAA+ protease YME1 gives insight into substrate processing. Science 358, 10.1126/science.aao0464 (2017).
34. Yokom AL et al. Spiral architecture of the Hsp104 disaggregase reveals the basis for polypeptide translocation. Nature Structural & Molecular Biology 23, 830–837, 10.1038/nsmb.3277 (2016).
35. Seyffer F et al. Hsp70 proteins bind Hsp100 regulatory M domains to activate AAA plus disaggregase at aggregate surfaces. Nature Structural & Molecular Biology 19, 1347-+, 10.1038/nsmb.2442 (2012).

36. Lipinska N et al. Disruption of Ionic Interactions between the Nucleotide Binding Domain 1 (NBD1) and Middle (M) Domain in Hsp100 Disaggregase Unleashes Toxic Hyperactivity and Partial Independence from Hsp70. J Biol Chem 288, 2857–2869, 10.1074/jbc.M112.387589 (2013). [PubMed: 23233670]
37. Elsworth B et al. Proteomic analysis reveals novel proteins associated with the Plasmodium protein exporter PTEX and a loss of complex stability upon truncation of the core PTEX component, PTEX150. Cell Microbiol 18, 1551–1569, 10.1111/cmi.12596 (2016). [PubMed: 27019089]
38. Kulzer S et al. Plasmodium falciparum-encoded exported hsp70/hsp40 chaperone/co-chaperone complexes within the host erythrocyte. Cell Microbiol 14, 1784–1795, 10.1111/j.1462-5822.2012.01840.x (2012). [PubMed: 22925632]
39. Batinovic S et al. An exported protein-interacting complex involved in the trafficking of virulence determinants in Plasmodium-infected erythrocytes. Nat Commun 8, 16044, 10.1038/ncomms16044 (2017). [PubMed: 28691708]
40. Adjalley SH et al. Quantitative assessment of Plasmodium falciparum sexual development reveals potent transmission-blocking activity by methylene blue. P Natl Acad Sci USA 108, E1214–E1223, 10.1073/pnas.1112037108 (2011).
41. Klemba M, Beatty W, Gluzman I & Goldberg DE Trafficking of plasmepsin II to the food vacuole of the malaria parasite Plasmodium falciparum (vol 164, pg 47, 2004). Journal of Cell Biology 164, 625–625, 10.1083/jcb.2004021616447 (2004).
42. Spillman NJ, Beck JR, Ganesan SM, Niles JC & Goldberg DE The chaperonin TRiC forms an oligomeric complex in the malaria parasite cytosol. Cell Microbiol 19, 10.1111/cmi.12719 (2017).
43. Scheres SHW A Bayesian View on Cryo-EM Structure Determination. J Mol Biol 415, 406–418, 10.1016/j.jmb.2011.11.010 (2012). [PubMed: 22100448]
44. Scheres SHW RELION: Implementation of a Bayesian approach to cryo-EM structure determination. J Struct Biol 180, 519–530, 10.1016/j.jsb.2012.09.006 (2012). [PubMed: 23000701]
45. Zheng SQ et al. MotionCor2: anisotropic correction of beam-induced motion for improved cryo-electron microscopy. Nat Methods 14, 331–332, 10.1038/nmeth.4193 (2017). [PubMed: 28250466]
46. Rohou A & Grigorieff N CTFFIND4: Fast and accurate defocus estimation from electron micrographs. J Struct Biol 192, 216–221, 10.1016/j.jsb.2015.08.008 (2015). [PubMed: 26278980]
47. Zhang K Gautomatch: a GPU-accelerated program for accurate, fast, flexible and fully automatic particle picking from cryo-EM micrographs with or without templates (2016).
48. Punjani A, Rubinstein JL, Fleet DJ & Brubaker MA cryoSPARC: algorithms for rapid unsupervised cryo-EM structure determination. Nat Methods 14, 290-+, 10.1038/Nmeth.4169 (2017). [PubMed: 28165473]
49. Pettersen EF et al. UCSF chimera - A visualization system for exploratory research and analysis. J Comput Chem 25, 1605–1612, 10.1002/jcc.20084 (2004). [PubMed: 15264254]
50. Emsley P, Lohkamp B, Scott WG & Cowtan K Features and development of Coot. Acta Crystallogr D 66, 486–501, 10.1107/S0907444910007493 (2010). [PubMed: 20383002]
51. Coordinators NR Database resources of the National Center for Biotechnology Information. Nucleic Acids Res 44, D7–D19, 10.1093/nar/gkv1290 (2016). [PubMed: 26615191]
52. Aurrecoechea C et al. PlasmoDB: a functional genomic database for malaria parasites. Nucleic Acids Res 37, D539–D543, 10.1093/nar/gkn814 (2009). [PubMed: 18957442]
53. Kelley LA, Mezulis S, Yates CM, Wass MN & Sternberg MJE The Phyre2 web portal for protein modeling, prediction and analysis. Nat Protoc 10, 845–858, 10.1038/nprot.2015.053 (2015). [PubMed: 25950237]
54. Adams PD et al. PHENIX: a comprehensive Python-based system for macromolecular structure solution. Acta Crystallogr D 66, 213–221, 10.1107/S0907444909052925 (2010). [PubMed: 20124702]
55. Chen VB et al. MolProbity: all-atom structure validation for macromolecular crystallography. Acta Crystallogr D 66, 12–21, 10.1107/S0907444909042073 (2010). [PubMed: 20057044]
56. Schrodinger LLC. The PyMOL Molecular Graphics System, Version 1.8 (2015).

57. Kucukelbir A, Sigworth FJ & Tagare HD Quantifying the local resolution of cryo-EMEM density maps. Nat Methods 11, 63-+, 10.1038/Nmeth.2727 (2014). [PubMed: 24213166]

58. Ganesan SM et al. Yeast dihydroorotate dehydrogenase as a new selectable marker for Plasmodium falciparum transfection. Mol Biochem Parasit 177, 29–34, 10.1016/j.molbiopara.2011.01.004 (2011).

59. Blisnick T et al. Pfsbp 1, a Maurer's cleft Plasmodium falciparum protein, is associated with the erythrocyte skeleton. Mol Biochem Parasit 111, 107–121, 10.1016/S0166-6851(00)00301-7 (2000).

60. Smart OS, Neduvelil JG, Wang X, Wallace BA & Sansom MSP HOLE: A program for the analysis of the pore dimensions of ion channel structural models. J Mol Graph Model 14, 354-&, 10.1016/S0263-7855(97)00009-X (1996).

61. Puchades C et al. Structure of the mitochondrial inner membrane AAA plus protease YME1 gives insight into substrate processing. Science 358, 609-+, 10.1126/science.aao0464 (2017).

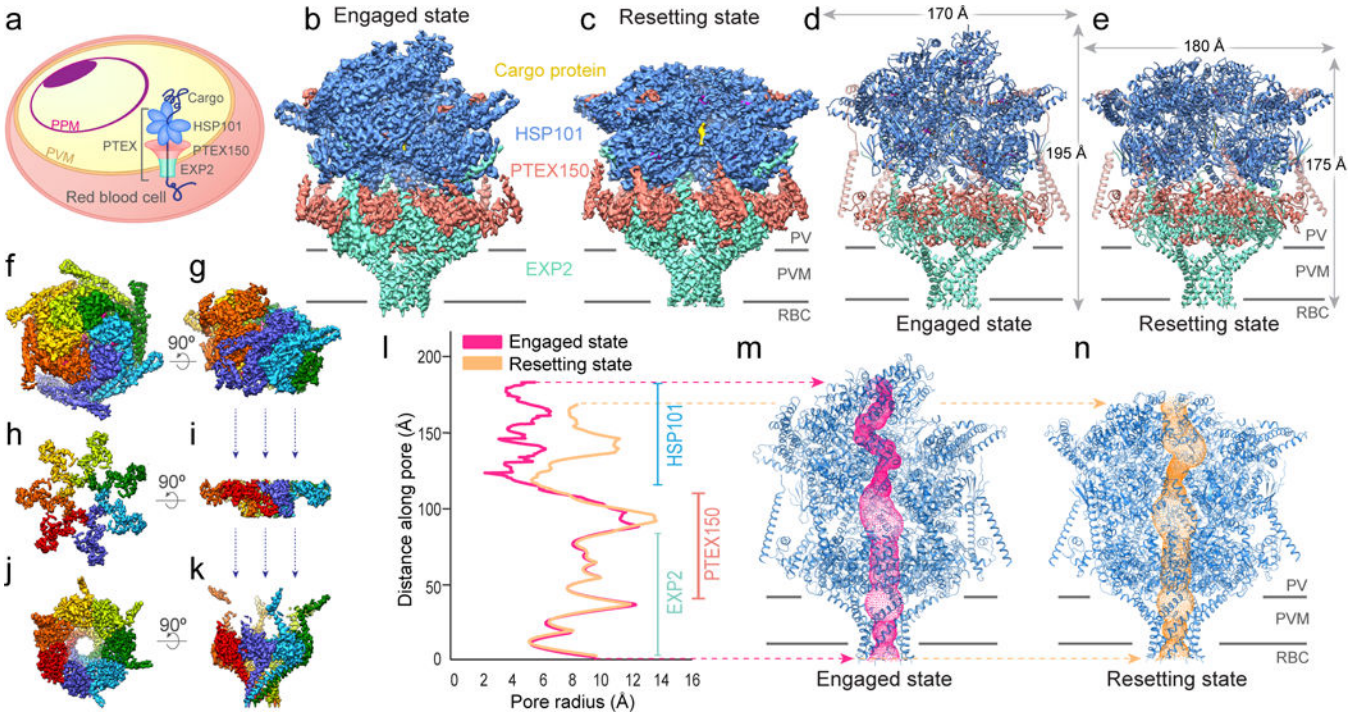

Figure 1. Global architecture of the PTEX core complex in two cargo-bound states.

a, Schematic of parasite-infected human erythrocyte. PPM: parasite plasma membrane. **b-e**, CryoEM maps (**b-c**) and atomic models (**d-e**) of the PTEX core complex. Horizontal lines represent the PVM bilayer, estimated based on the detergent belt density, visible at lower thresholds (see Extended Data Fig. 7). **f-k**, Top and side views of the HSP101 (**f-g**), PTEX150 (**h-i**), and EXP2 (**j-k**) cryoEM maps, coloured by protomer. **l-n**, Pore radius (**l**) and protein-conducting channel (**m-n**) calculated using HOLE[60].

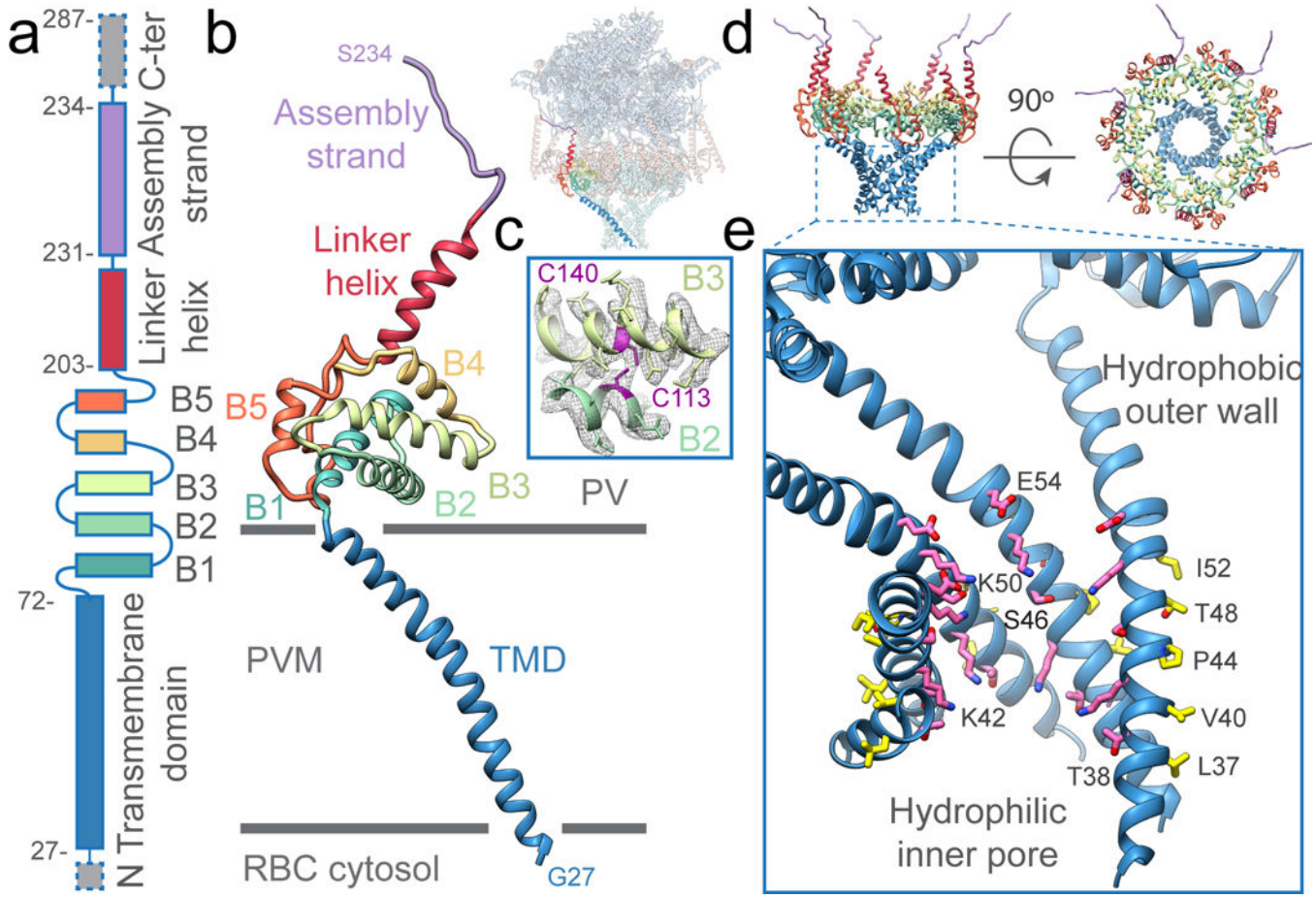

Figure 2. EXP2 forms a heptameric pseudo-symmetric PVM-spanning pore.

a,b Linear schematic (**a**) and ribbon diagram (**b**) of the EXP2 monomer in the *engaged* state. Dashed gray boxes represent unmodeled regions. Inset: one EXP2 monomer (coloured) within the PTEX complex. **c**, Density (mesh) and model of C113-C140 disulfide bond. **d**, EXP2 heptamer, coloured as in **(b)**. **e**, Cutaway of the EXP2 transmembrane channel with hydrophilic residues (pink) lining the inner protein-conducting pore and hydrophobic residues (yellow) on the outer, membrane-facing surface.

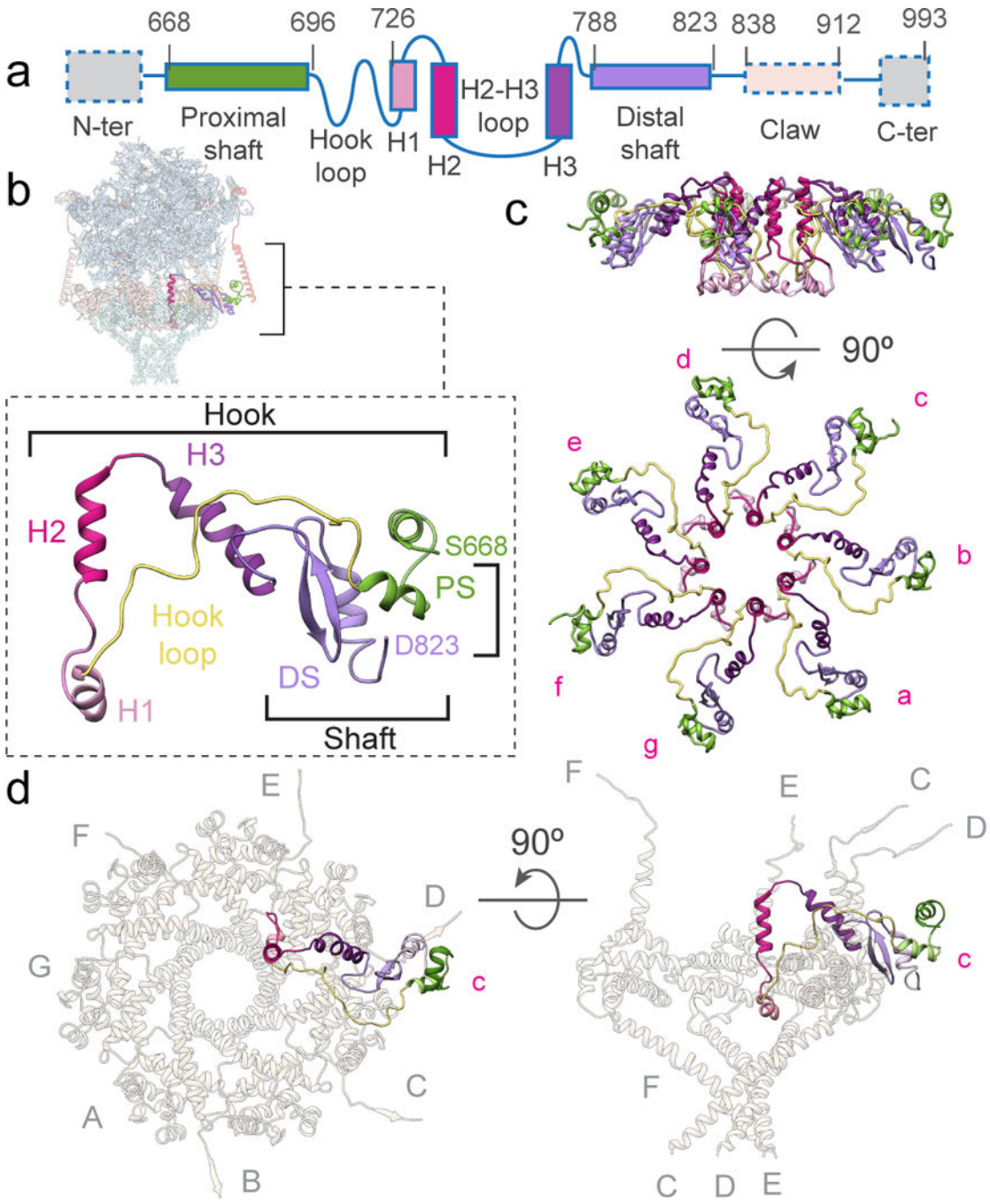

Figure 3. PTEX150 forms a heptameric flange-shaped adaptor between EXP2 and HSP101.

a,b Linear schematic (**a**) and ribbon diagram (**b**) of the PTEX150(668–823) monomer in the *engaged* state. Dashed gray boxes represent unmodeled regions. Inset: one PTEX150(668–823) monomer (coloured) within the PTEX complex. PS, proximal shaft; DS, distal shaft. **c**, The PTEX150(668–823) heptamer, colored as in **(b)**. **d**, Views showing how one PTEX150(668–823) monomer hooks into the top of the EXP2 funnel.

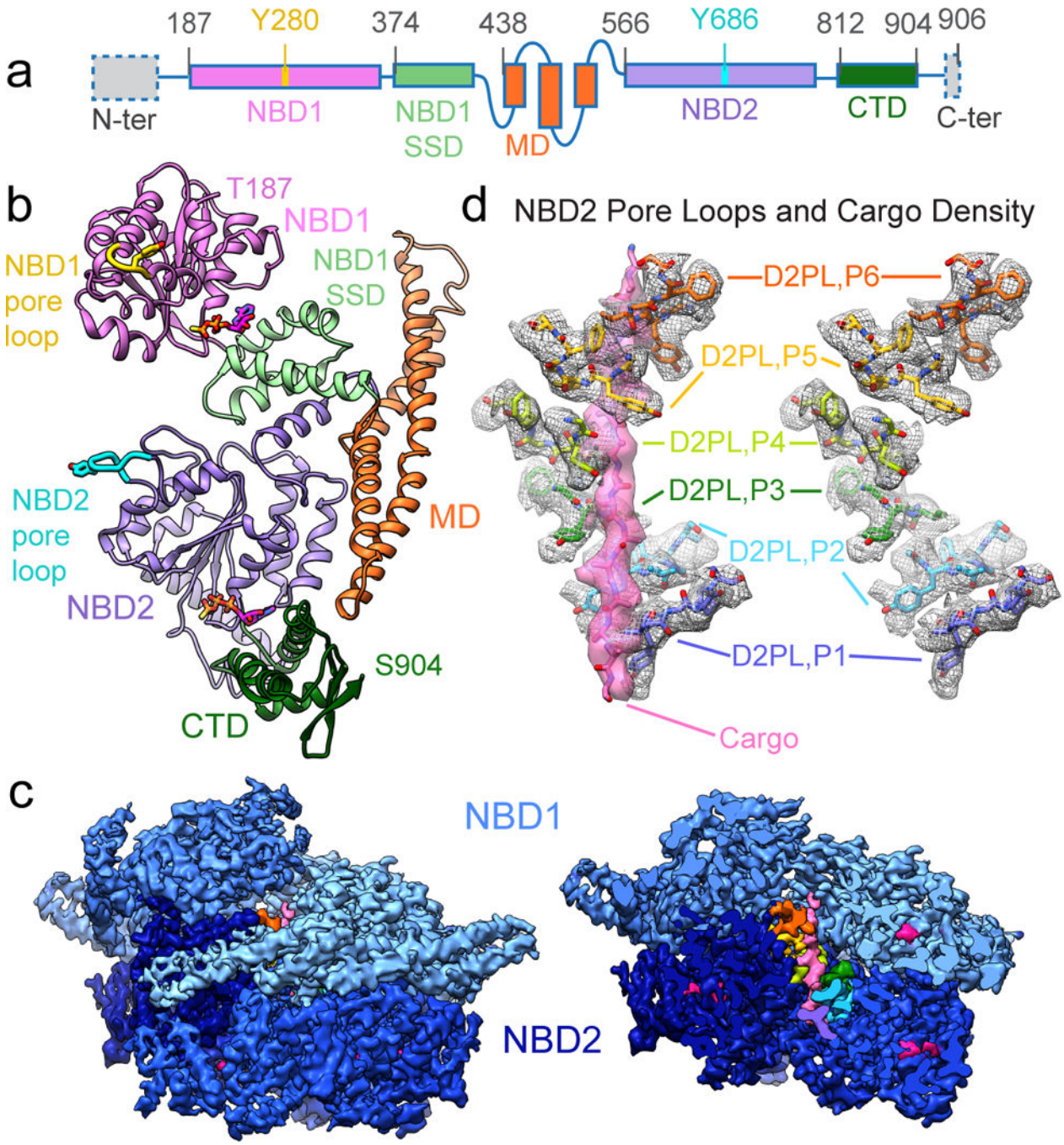

Figure 4. Endogenous cargo bound in the channel of the HSP101 hexamer.

a,b Linear schematic (**a**) and ribbon diagram (**b**) of the HSP101 monomer in the *engaged* state. **c**, Side view of the full (left) and bisected (right) HSP101 hexamer cryoEM map. NBD1 and NBD2 rings are coloured with light (NBD1) and dark (NBD2) blue gradients to emphasize the right-handed spiral shape of the hexamer. In the bisected map, NBD2 pore loop densities are coloured by protomer, ATPγS is colored magenta, and the cargo density is colored light pink. **d**, Enlarged side view of the atomic models of the HSP101 NBD2 pore loops and unfolded cargo polypeptide backbone, shown with densities. NBD2 pore loops are

colored as in (**c**) and labeled by protomer (e. g., D2PL,P1: NBD2 Pore Loop, Protomer 1). Vertical distances between pore loop tyrosines in D2PL,P1–6 are 6.52Å, 6.28Å, 6.38Å, 6.96Å and 6.12Å, respectively.

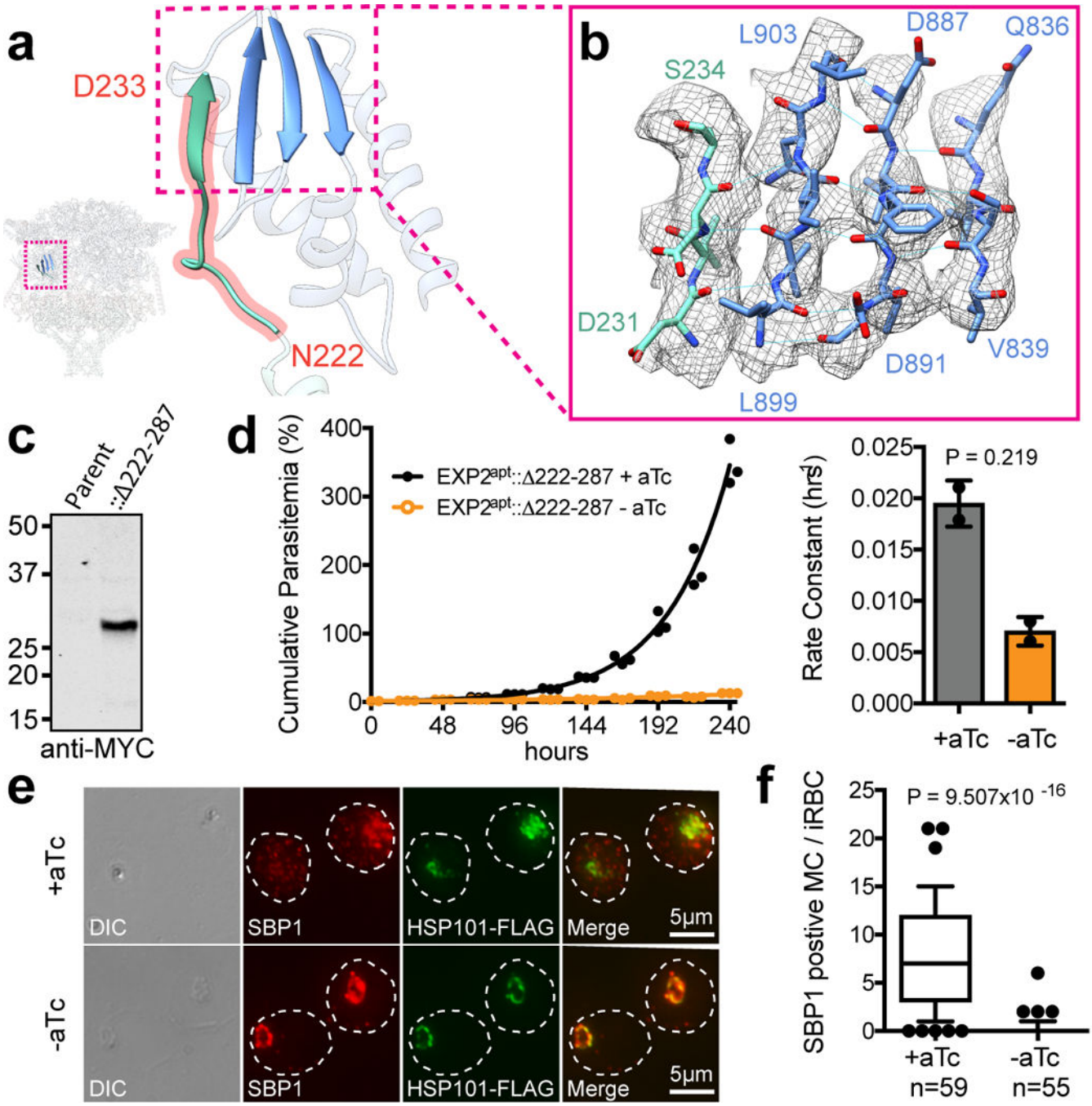

Figure 5. Interactions essential to PTEX function.

a,b Ribbon (**a**) and stick (**b**) models of the HSP101 CTD β-sheet augmented by the EXP2 assembly strand, shown with corresponding cryoEM density (mesh). Segment outlined in red was truncated in functional complementation assays. **c**, Western blot of EXP2^{apt} parasites complemented with EXP2Δ222–287-3xMYC (predicted molecular weight: 27.8 kDa after signal peptide cleavage). For blot source data, see Supplementary Fig. 1. **d**, Growth analysis of EXP2^{apt}::Δ222–287-3xMYC. Parasites were grown with or without aTc to maintain or knockdown endogenous EXP2 expression, respectively. One experiment

performed with three technical replicates is shown. Bar graph shows mean exponential growth rate constant (hr^{-1}) determined from the fit of the two independent experiments and error bars indicate s.d. **e**, Immunofluorescence assay (IFA) detecting exported protein SBP1 and HSP101–3xFLAG (as a PV marker) in $EXP2^{apt}$::Δ222–287-3xMYC parasites allowed to develop with or without aTc to 24 hr post invasion. Dashed line indicates the traced boundary of the RBC. DIC, differential interference contrast. **f**, Quantification of SBP1 export IFA assays. Data are pooled from two independent experiments, *n* is the number of individual parasite-infected RBCs. Boxes and whiskers delineate 25th-75th and 10th-90th percentiles, respectively. All *P* values determined by an unpaired, two-sided t-test. All data shown represent two independent experiments.

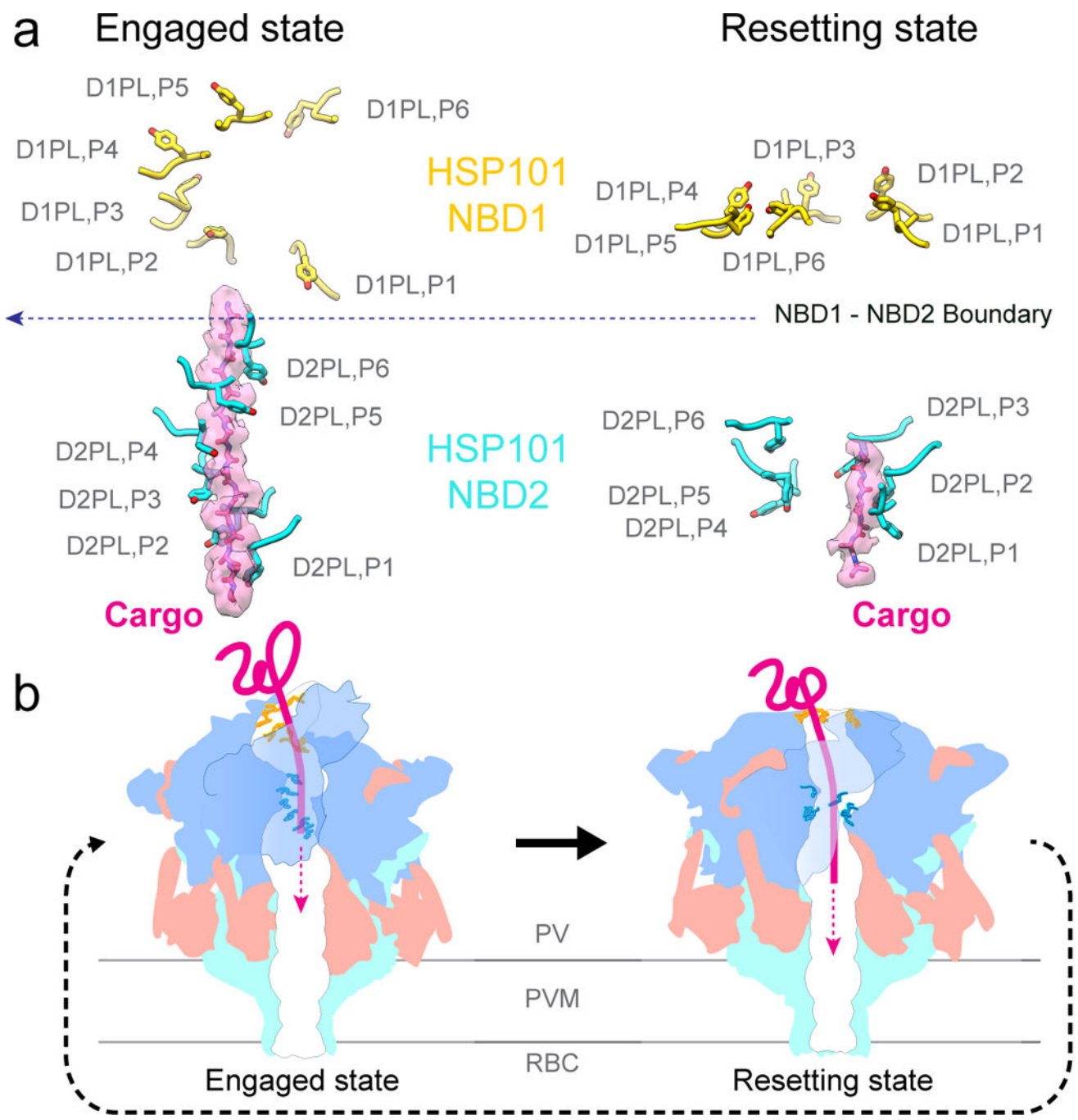

Figure 6. Mechanism of translocation.

a, Side views of the HSP101 pore loops with the unfolded cargo peptide backbone models (pink) built into the cryoEM densities (pink). Vertical distances between pore loop tyrosines in consecutive loops are: *engaged* D1PL,P1–6: 9.41Å, 8.61Å, 1.40Å, 3.34Å, 2.28Å; *engaged* D2PL,P1–6: 6.52Å, 6.28Å, 6.38Å, 6.96Å, 6.12Å; *resetting* D1PL,P1–6: 1.75Å, −2.70Å, −1.65Å, −0.78Å, 1.81Å; *resetting* D2PL,P1–6: 5.88Å, 4.56Å, −6.80Å, 2.25Å, 7.88Å. **b**,

Proposed stepwise feeding mechanism of translocation by PTEX. NBD1 and NBD2 pore loops and cargo are colored as in (**a**).